

AD-A020 711

PASSIVE NOSETIP TECHNOLOGY (PANT) PROGRAM. VOLUME
XIII. AN EXPERIMENTAL STUDY TO EVALUATE HEAT
TRANSFER RATES TO SCALLOPED SURFACES - DATA REPORT

T. C. Derbidge, et al

Acurex Corporation

Prepared for:

Space and Missile Systems Organization

April 1974

DISTRIBUTED BY:

NTIS

National Technical Information Service
U. S. DEPARTMENT OF COMMERCE

055043

SAMSO-TR-74-86
Volume XIII

1

ADA020711

INTERIM REPORT
PASSIVE NOSETIP TECHNOLOGY
(PANT) PROGRAM

Volume XIII. An Experimental Study to Evaluate Heat
Transfer Rates to Scalloped Surfaces -
Data Report

T. C. Derbidge
M. R. Wool

Aerotherm Division/Acurex Corporation

SAMSO-TR-74-86

April 1974

AERTHERM REPORT 74-100

DDC
RECEIVED
FEB 17 1976
AT

This document may be distributed further by any holder
only with specific prior approval of Space and Missile
Systems Organization (SAMSO), Los Angeles, California.

Air Force Space and Missile
Systems Organization
Los Angeles, California

DISTRIBUTION STATEMENT A
Approved for public release:
Distribution Unlimited

Contract F04701-71-C-0027

Reproduced by
NATIONAL TECHNICAL
INFORMATION SERVICE
U S Department of Commerce
Springfield VA 22151

Vol. 13 - AL 50 710

SAMSO-TR-74-86
Volume XIII

C/N 7045.423

INTERIM REPORT
PASSIVE NOSETIP TECHNOLOGY
(PANT) PROGRAM

Volume XIII. An Experimental Study to Evaluate Heat
Transfer Rates to Scalloped Surfaces —
Data Report

T. C. Derbidge
M. R. Wool

This document may be distributed further by holder
only with specific prior approval of Space and Missile
System Organization (SAMSO), Los Angeles, California.

DISTRIBUTION STATEMENT A
Approved for public release;
Distribution Unlimited

FOREWORD

Handwritten: Put in file

ACCESSION FOR	NTIS	DTIC	US GOVERNMENT PRINTING OFFICE	BY	DATE	CLASS	COMMENTS

This document is Volume XIII of the Interim Report series for the Passive Nosetip Technology (PANT) program. A summary of the documents in this series prepared to date is as follows:

- Volume I - Program Overview (U)
- Volume II - Environment and Material Response Procedures for Nosetip Design (U)
- Volume III - Surface Roughness Data
 - Part I - Experimental Data
 - Part II - Roughness Augmented Heating Data Correlation and Analysis (U)
 - Part III - Boundary Layer Transition Data Correlation and Analysis (U)
- Volume IV - Heat Transfer and Pressure Distributions on Ablated Shapes
 - Part I - Experimental Data
 - Part II - Data Correlation
- Volume V - Definition of Shape Change Phenomenology from Low Temperature Ablator Experiments
 - Part I - Experimental Data, Series C (Preliminary Test Series)
 - Part II - Experimental Data, Series D (Final Test Series)
 - Part III - Shape Change Data Correlation and Analysis
- Volume VI - Graphite Ablation Data Correlation and Analysis (U)
- Volume VII - Computer User's Manual, Steady-State Analysis of Ablating Nosetips (SAANT) Program
- Volume VIII - Computer User's Manual, Passive Graphite Ablating Nosetip (PAGAN) Program
- Volume IX - Unsteady Flow on Ablated Nosetip Shapes - PANT Series G Test and Analysis Report

- Volume X - Summary of Experimental and Analytical Results
- Volume XI - Analysis and Review of the ABRES Combustion Test Facility for High Pressure Hyperthermal Reentry Nosetip Systems Tests
- Volume XII - Nosetip Transition and Shape Change Tests in the AFFDL 50 MW RENT Arc - Data Report
- Volume XIII - An Experimental Study to Evaluate Heat Transfer Rates to Scalloped Surfaces - Data Report
- Volume XIV - An Experimental Study to Evaluate the Irregular Nosetip Shape Regime - Data Report
- Volume XV - Roughness Induced Transition Experiments - Data Report

This report was prepared by Aerotherm Division/Acurex Corporation under Contract F04701-71-C-0027. Volumes I through IX covered PANT activities from April 1971 through April 1973. Volumes X through XV represent contract efforts from May 1973 to December 1974. Volume X summarizes the respective test programs and describes improvements in nosetip analysis capabilities. Volume XI presents an evaluation of the ABRES test facility in terms of performing thermostructural and reentry flight simulation testing. Volumes XII through XV are data reports which summarize the experiments performed for the purpose of defining the irregular flight regime. The analysis of these data are presented in Volume X.

This work was administered under the direction of the Space and Missile Systems Organization with Lieutenant A. T. Hopkins and Lieutenant E. G. Taylor as Project Officers with Mr. W. Portenier and Dr. R. L. Baker of the Aerospace Corporation serving as principal technical monitors. T. C. Derbidge was the Aerotherm principal investigator and the test engineer for tests described in this volume

This technical report has been reviewed and is approved.

E G Taylor

E. G. Taylor, Lt., USAF
Project Officer
Aero and Materials Division
Directorate of Systems Engineering
Deputy for Reentry Systems

ABSTRACT

Hypersonic wind tunnel tests conducted in the Naval Ordnance Laboratory Tunnel Number 8 are described. One calorimeter model which was an exact replica of a scalloped low-temperature-ablator nosetip model was tested at Mach 5, with a total temperature of 830°R and freestream unit Reynolds numbers from 2×10^6 to $21 \times 10^6/\text{ft}$. Measured heat transfer rates are 1.5 to 2.3 times corresponding smooth wall turbulent predictions. Heating data agree nominally with heat transfer rates inferred from the ablation test results. It is conjectured that scallops increase surface heating through effects on the shock layer flow.

TABLE OF CONTENTS

<u>Section</u>		<u>Page</u>
1	INTRODUCTION	1-1
2	TEST OBJECTIVES	2-1
3	MODEL DESCRIPTION	3-1
	3.1 Calorimeter Model and Instrumentation	3-1
	3.2 Determination of Effective Wall Thickness	3-5
	3.3 Calorimeter Thermal Properties	3-7
4	TEST MATRIX	4-1
5	DESCRIPTION OF RECORDED DATA	5-1
6	TEST RESULTS	6-1
	6.1 Definition of Calorimeter Heat Flux and Heat Transfer Coefficient	6-1
	6.2 Data Reduction	6-17
	6.3 Heat Flux and Heat Transfer Coefficient Distributions	6-17
7	RESULTS AND CONCLUSIONS	7-1
	7.1 Comparison with Inferred Heating	7-1
	7.2 Comparison with PANT Rough Wall Heating Correlation	7-6
	7.3 Conclusions and Recommendations	7-11
	REFERENCES	R-1

LIST OF FIGURES

<u>Figure</u>		<u>Page</u>
3-1	Calorimeter Model Configuration	3-2
3-2	Definition of Thermocouple Locations	3-4
4-1	Nominal Test Points at $M_\infty = 5.0$ in NOL Hypersonic Wind Tunnel	4-2
5-1	Sample of Measured Thermocouple Histories	5-2
5-2	Sample Shadowgraph Photographs	5-8
6-1	Cross-section Schematic of Typical Aluminum/Epoxy/RTV Interaction	6-2
6-2	Schematic of Computer Models Used to Represent the Aluminum/RTV and Aluminum/Epoxy Interfaces	6-4
6-3	Typical Calculated Heat Flux Histories	6-6
6-4	Typical Ratio of Conducted to Convected Heat Rate Versus Time	6-8
6-5	Comparison of Two Different Conduction Loss Calculations When Plotted Versus Correlation Parameters	6-10
6-6	Conduction Loss Terms Plotted Versus Correlation Parameters	6-11
6-7	Predicted Pressure Distribution for the Scallop Calorimeter	6-14
6-8	Predicted Recovery Temperature Distribution for the Scallop Calorimeter	6-15
6-9	Measured Shock Shape for Run 502 ($Re_\infty = 10.93 \times 10^6/\text{ft}$, $M_\infty = 5$)	6-16
6-10	Comparison of Typical Thermocouple Response to Suspicious Thermocouple Response	6-18
6-11	Incident Heat Flux Distribution, Scallop Calorimeter Model	6-20
6-12	Convective Heat Transfer Coefficient Distribution, Scallop Calorimeter Model	6-27
7-1	Surface Slope Distribution for the Final Shape of Run 201	7-3
7-2	Measured Recession Rates and Best Estimate of Normal Recession Rate Distribution for the Final Time of Run 201	7-4
7-3	Inferred Distribution of Nonblown Heat Transfer Coefficient for the Final Shape of Run 201	7-5
7-4	Comparison of Inferred and Measured Heat Transfer Coefficient Distribution for the Baseline Reynolds Number Condition (Run 502)	7-7
7-5	Comparison of the Series H Calorimeter Data with the PANT Roughwall Heating Correlation	7-9

LIST OF TABLES

<u>Table</u>		<u>Page</u>
3-1	Nominal Surface Coordinates of PANT Series H Scallop Replica Calorimeter Model	3-3
3-2	Determination of Effective Wall Thickness for Scallop Calorimeter	3-6
3-3	Summary of Measured Cast Aluminum Material Properties	3-7
4-1	Test Conditions for PANT Series H Wind Tunnel Tests - February 1974	4-3
6-1	Nominal Thermal Properties for Calorimeter Calculations	6-5
6-2	Calculated Conduction/Convection Ratios at Time = 1.0 Second	6-9

LIST OF SYMBOLS

C	specific heat
C_{Hs}	smoothwall Stanton number
d_1	ring diameter
d_2	
h or HTC	convective heat transfer coefficient
k	thermal conductivity
L	ring width
M	Mach number
P	pressure
Pr	Prandlt number
\dot{q}	heat flux
R	shock radius
Re	Reynolds number
R_f	recovery factor
S	surface distance
\dot{s}	normal surface recession rate
t	ring thickness

t_{TP}	thermal penetration depth
T	temperature
u	velocity
α	thermal diffusivity
β	shock angle
δ_{SL}	laminar sublayer thickness
θ	time
μ	viscosity
ρ	density

Subscripts

AL	aluminum
conv	convected heat transfer
e	boundary layer edge property
i	initial condition
o	supply conditions
r	boundary layer recovery property
RTV	room-temperature-vulcanizing rubber
t_2	total conditions down stream of a normal shock
w	property evaluated at wall conditions
∞	free stream property

SECTION 1

INTRODUCTION

The overall objective of the PANT program (Contract F04701-71-C-0027) is to improve and validate the accuracy of existing nosetip design analysis computer codes. Task 4.2.5 of the PANT program has the objective of defining the environmental regimes which produce irregular nosetip shapes and updating nosetip design analysis codes. In order to satisfy this objective a series of wind tunnel and high pressure ablation tests was required. The tests were designed to obtain calorimeter and shape change data for geometries and environments of interest. The objectives of the four test series are given below.

50 MW Arc Heater Tests - Test ATJ-S graphite, Mod-III carbon/carbon, and reverse chevron carbon phenolic nosetip models in the 50 MW arc using a $M_\infty = 3$ nozzle to assess the transition behavior and shape change response of "real" materials in a hyperthermal environment.

Series H Wind Tunnel Tests - Generate heat transfer data for a calorimeter replica of an LTA scallop roughened surface for comparison with inferred heat transfer data and predictions.

Series I Wind Tunnel Tests - Generate low temperature ablator (LTA) shape change data to determine the effect of relevant nosetip parameters on the formation and extent of irregular shapes.

Series J Wind Tunnel Tests - Generate heat transfer data which show the effect of surface roughness and model size on boundary layer transition and augmentation of smooth wall heat flux.

The 50 MW tests were conducted in the RENT leg of the 50 MW arc facility at the Air Force Materials Flight Dynamics Laboratory. Test series H and J were conducted in Tunnel No. 8 at the Naval Ordnance Laboratory (NOL) from February 21 to February 26, 1974. Test Series I was conducted at NOL from March 27 to April 4, 1974.

These test series compliment Series E and G which were directed at obtaining pressure data on nosetips of irregular shape. A brief description of these two test series is given below:

Series E (Task 4.2.3) - Generate high frequency pressure, acceleration, and shock shape stability data to establish the possibility of high frequency flow field pulsations on ablated nosetip shapes.

Series G (Task 4.2.7) - Generate high frequency pressure, acceleration, and shock shape stability data to determine the envelope of realistic nosetip shapes which induce high frequency flow field pulsations.

Test Series E and G were conducted in NOL Tunnel No. 8; Series E was conducted in October of 1972 and Series G was conducted from July 25 to August 1, 1973. The results of Series G are reported in Reference 1.

This data report presents the results of Test Series H. The test objectives are defined in Section 2, the model and apparatus are described in Section 3, the matrix of tests conducted is presented in Section 4, a description of the recorded data is given in Section 5, the test results are presented in Section 6, and conclusions are discussed in Section 7.

SECTION 2

TEST OBJECTIVES

The experimental program was directed at accomplishing the following objectives:

1. Generate heat transfer data for a calorimeter replica of an ablated LTA scallop roughened surface for comparison with heat transfer data inferred from the recession rate of the LTA model.
2. Generate heat transfer data for a scallop calorimeter model over a range of Reynolds numbers for comparison with current prediction techniques.

The above objectives were accomplished by exposing one calorimeter scallop replica model to several Reynolds number conditions in the NOL No. 8 hypersonic wind tunnel at a free stream Mach number of 5. The first objective was accomplished by testing a calorimeter model which is a replica of the final shape of PANT Series D LTA model 201 at the same Reynolds number condition at which model 201 was tested ($Re_\infty = 10 \times 10^6/\text{ft}$).

The second objective was accomplished by testing the same calorimeter replica model over a range of Reynolds numbers as indicated in the test matrix (Section 4.)

SECTION 3

MODEL DESCRIPTION

The calorimeter model used in these tests measures convective heat flux to a surface which is a replica of an ablated nosetip surface. The determination of heat flux is based upon the measurement of the temperature history of an isolated thermal capacitance element. Heat flux is inferred from this temperature history by application of the law of conservation of energy. Thermal properties, thermocouple locations and calorimeter wall thickness are other quantities needed to evaluate the heat flux.

A description of the calorimeter construction and instrumentation is given in Section 3.1, the determination of effective wall thickness is described in Section 3.2, and the measured calorimeter thermal properties are presented in Section 3.3

3.1 CALORIMETER MODEL AND INSTRUMENTATION

The calorimeter model is a replica of the final ablated shape of Run 201 of the PANT Series D low temperature ablator tests. The configuration of the calorimeter model is shown in Figure 3-1. A table of the nominal surface coordinates used for data reduction and predictions is given in Table 3-1. A further discussion of the definition of the nominal surface profile, the limits of uncertainty, and the effect on predicted heating is given in Section 7. The thermal capacitance elements are cast aluminum segments of a shell. The aluminum segments are held together and insulated from one another with HP550 Epoxy, which is a high temperature glass filled epoxy. One segment is a 1.3 inch diameter nose cap. The remaining four segments are rings. Near the stagnation point, the width of the first two rings is 0.55 and 0.65 inches, respectively. Further downstream the width of the last two rings is 0.97 and 1.32 inches, respectively. For measurement of temperature history, the aluminum segments are instrumented with a total of 18 thermocouples constructed of 36 gauge (0.5 mil) chromel and alumel wire. Figure 3-2 indicates the thermocouple locations.

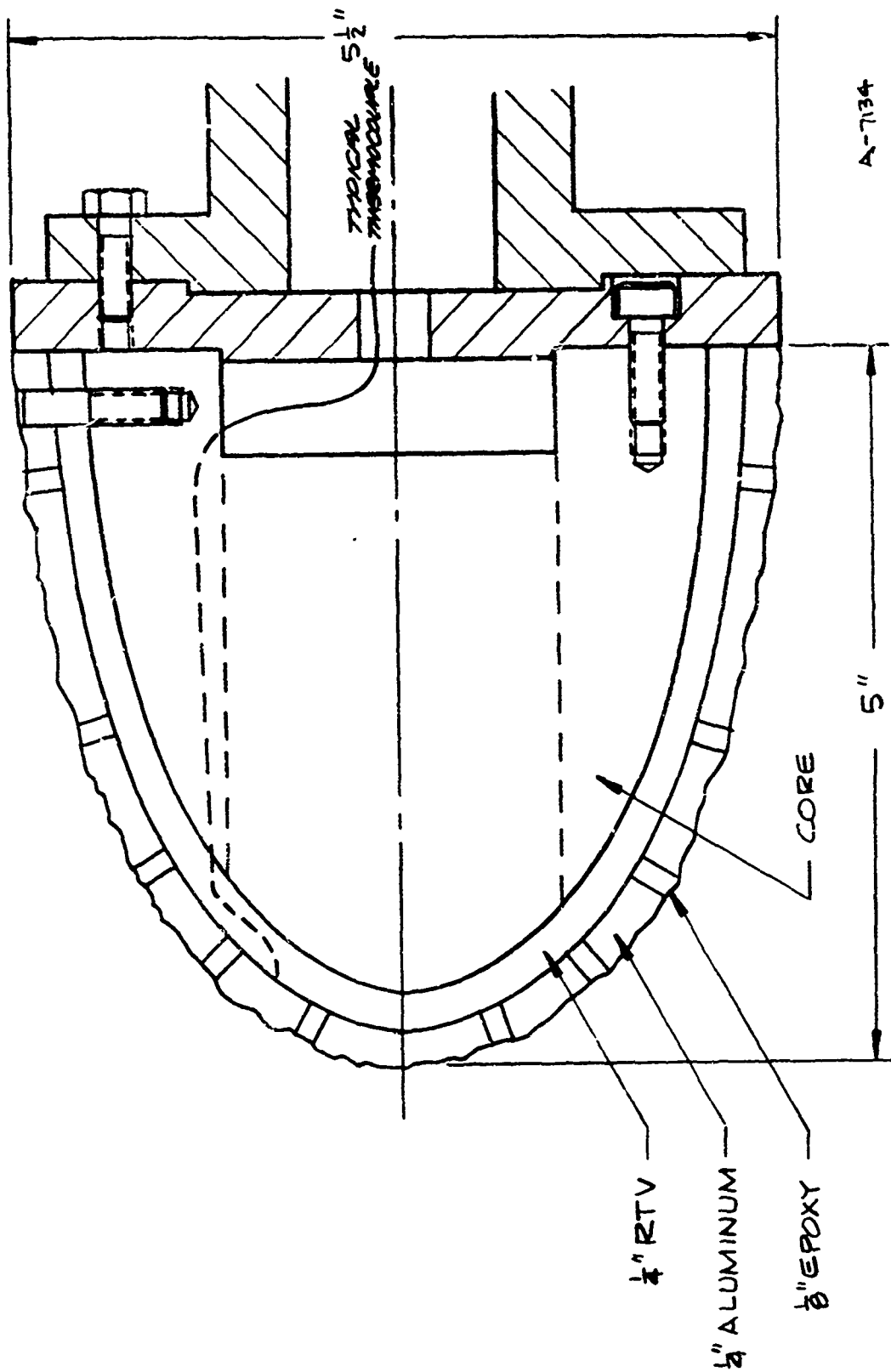


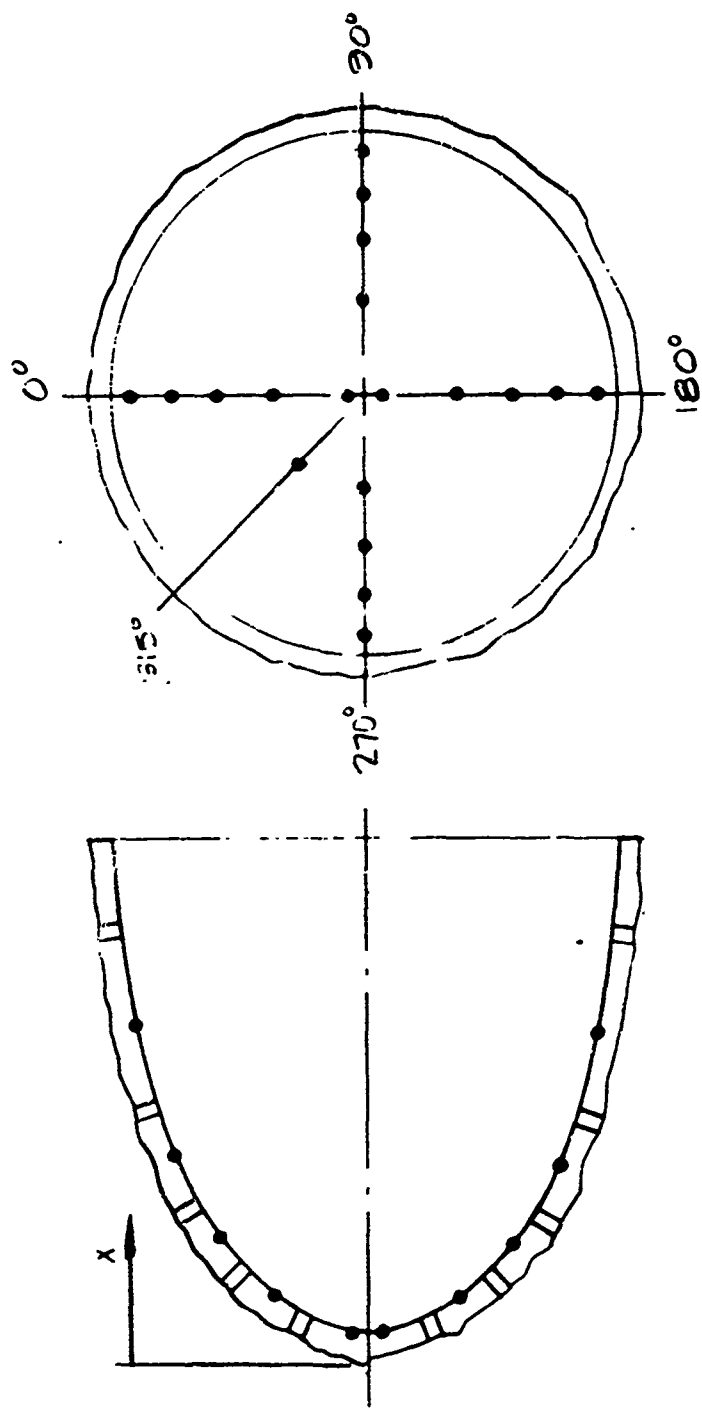
Figure 3-1. Calorimeter Model Configuration

TABLE 3-1

NOMINAL SURFACE COORDINATES OF PANT SERIES H SCALLOP REPLICA
CALORIMETER MODEL

No.	Axial Length x (in.)	Radial Length y (in.)	Stream Length s (in.)	Surface Slope* (deg)
1	0.0	0.0	0.0	90.0
2	0.008	0.042	0.043	64.0
3	0.040	0.110	0.118	63.7
4	0.090	0.217	0.236	62.3
5	0.140	0.325	0.355	61.3
6	0.151	0.345	0.378	61.0
7	0.190	0.420	0.462	60.3
8	0.290	0.599	0.667	58.3
9	0.390	0.750	0.848	56.3
10	0.490	0.905	1.033	54.8
11	0.586	1.036	1.196	52.5
12	0.590	1.041	1.202	52.5
13	0.690	1.176	1.370	50.4
14	0.790	1.299	1.528	48.5
15	0.890	1.413	1.680	46.4
16	0.990	1.522	1.828	44.3
17	1.067	1.597	1.935	42.5
18	1.090	1.619	1.967	41.9
19	1.190	1.701	2.097	39.9
20	1.250	1.760	2.181	38.3
21	1.550	2.000	2.565	36.0
22	1.926	2.235	3.008	28.0
23	2.350	2.410	3.467	21.5
24	2.750	2.525	3.883	17.6
25	3.178	2.650	4.329	15.5
26	3.650	2.770	4.816	14.1
27	4.100	2.890	5.282	13.3
28	4.550	3.010	5.748	13.0
29	5.000	3.140	6.216	12.6

* This slope is the average of the uncertainty band for each location.



A. SEPARATED BY APPROXIMATELY .25"
B. NOT FUNCTIONING

RADIAL LOCATION (IN)	AXIAL LOCATION (IN)	CIRCUMFERENTIAL LOCATION				
		0°	90°	180°	270°	315°
.345		1		2		
1.036		3	4	5	6	19°
1.597		7	8	9	10	
	1.91	11	12	13	14	
	3.179	15	16	17	18/20	

A-7135

Figure 3-2. Definition of Thermocouple Locations

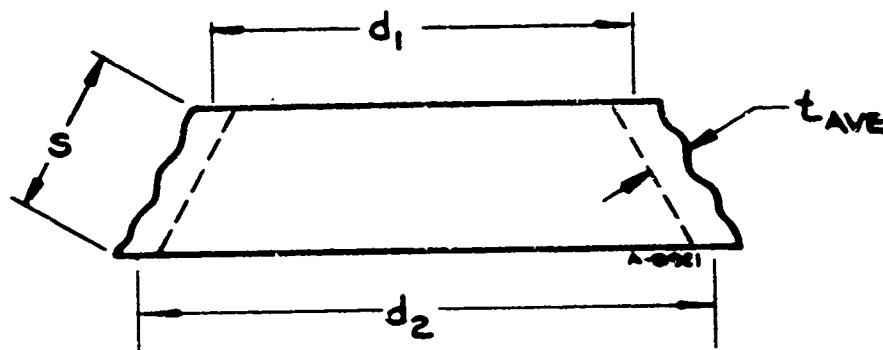
The segmented aluminum outer shell is supported by a hard wood central core. A layer of room-temperature-vulcanizing (RTV) silicon rubber insulates the segmented shell from the central core. The purposes of this RTV layer are to

- Provide insulation between the aluminum shell and the central core
- Provide an elastic interface to absorb any differential thermal expansion
- Immobilize and secure the thermocouple leads.

The aluminum and insulating layer are held to the central core by two bolts which allow thermal expansion of the two layers but do not extend outside the aluminum outer layer to interrupt the flow.

3.2 DETERMINATION OF EFFECTIVE WALL THICKNESS

The average effective wall thickness of each ring was determined by dividing the ring volume by the projected surface area. The volume was found by weighing the ring and dividing by the density which was measured from control casting specimens by Dynatech Corporation (Reference 2) as 168.6 lbm/ft³. The projected surface area was calculated assuming each ring to be approximated by a frustum of a cone as indicated in the following sketch.



$$\text{Projected area} = \left(\frac{d_1 + d_2}{2} \right) \pi S$$

The results of these calculations are summarized in Table 3-2.

The projected surface area of the small nose cap piece was calculated assuming it to be approximated by a cone. Due to the small size of the piece

TABLE 3-2
DETERMINATION OF EFFECTIVE WALL
THICKNESS FOR SCALLOP CALORIMETER

Ring No.	Dimensions			Weight (lb)	Average Thickness t_{ave} (inches)
	d_1	d_2 (inches)	S		
1	N/A*	1.300	0.763	0.0220	0.145
2	1.480	2.380	$0.555 \pm .005$	0.0550	$0.1665 \pm .0015$
3	2.545	3.320	$0.660 \pm .010$	0.1389	$0.2260 \pm .0030$
4	3.400	4.215	$0.970 \pm .020$	0.3210	$0.2830 \pm .0060$
5	4.310	4.965	$1.325 \pm .015$	0.5070	$0.2686 \pm .0030$

* Not applicable - nose cap

and the singular nature of the stagnation point there is greater uncertainty in the calculated projected area for the nose cap than for the other rings.

3.3 CALORIMETER THERMAL PROPERTIES

The thermal properties of the cast aluminum calorimeter material were determined by measurement of control specimens cast at the same time as the calorimeter shell. The measurements were performed by Dynatech Corporation and are described in Reference 2 and summarized in Table 3-3.

TABLE 3-3
SUMMARY OF MEASURED CAST
ALUMINUM MATERIAL PROPERTIES

Temperature (°F)	Specific Heat (Btu/lbm - °R)
32	0.2089
122	0.2191
212	0.2275
302	0.2354
392	0.2426

Thermal Conductivity =
0.02425 Btu/sec-ft-°R

Density = 168.6 lbm/ft³

SECTION 4

TEST MATRIX

The Series H wind tunnel tests were conducted in NOL Tunnel No. 8. The NOL Tunnel No. 8 is an intermittent blowdown hypersonic wind tunnel. For this tunnel, air is the working gas and is compressed and stored in high pressure containers. In transit to the nozzle, this air is heated to the desired supply temperature by passing it through a pebble bed heater. The tunnel has an open pit test section and a constant area diffuser. The Mach number selected for this test series is $M_\infty = 5$. The associated nozzle has a rectangular cross section with throat dimensions of 0.6398 inch x 16.000 inch and exit dimension of 17.37 inch x 16.97 inch.

At a Mach number of 5, the Reynolds number operating envelope for Tunnel No. 8 is presented in Figure 4-1 as a function of supply temperature (T_0) and supply pressure (P_0). Superimposed on this figure are the nominal operating conditions for the calorimeter. As shown by Figure 4-1, all of the nominal test conditions for the calorimeter are at a stagnation temperature of 400°F and supply pressures corresponding to free stream Reynolds numbers of 2.5, 5, 7.5, 10, 15 and 20 x 10⁶/ft, respectively. The actual average measured conditions are presented in Table 4-1.

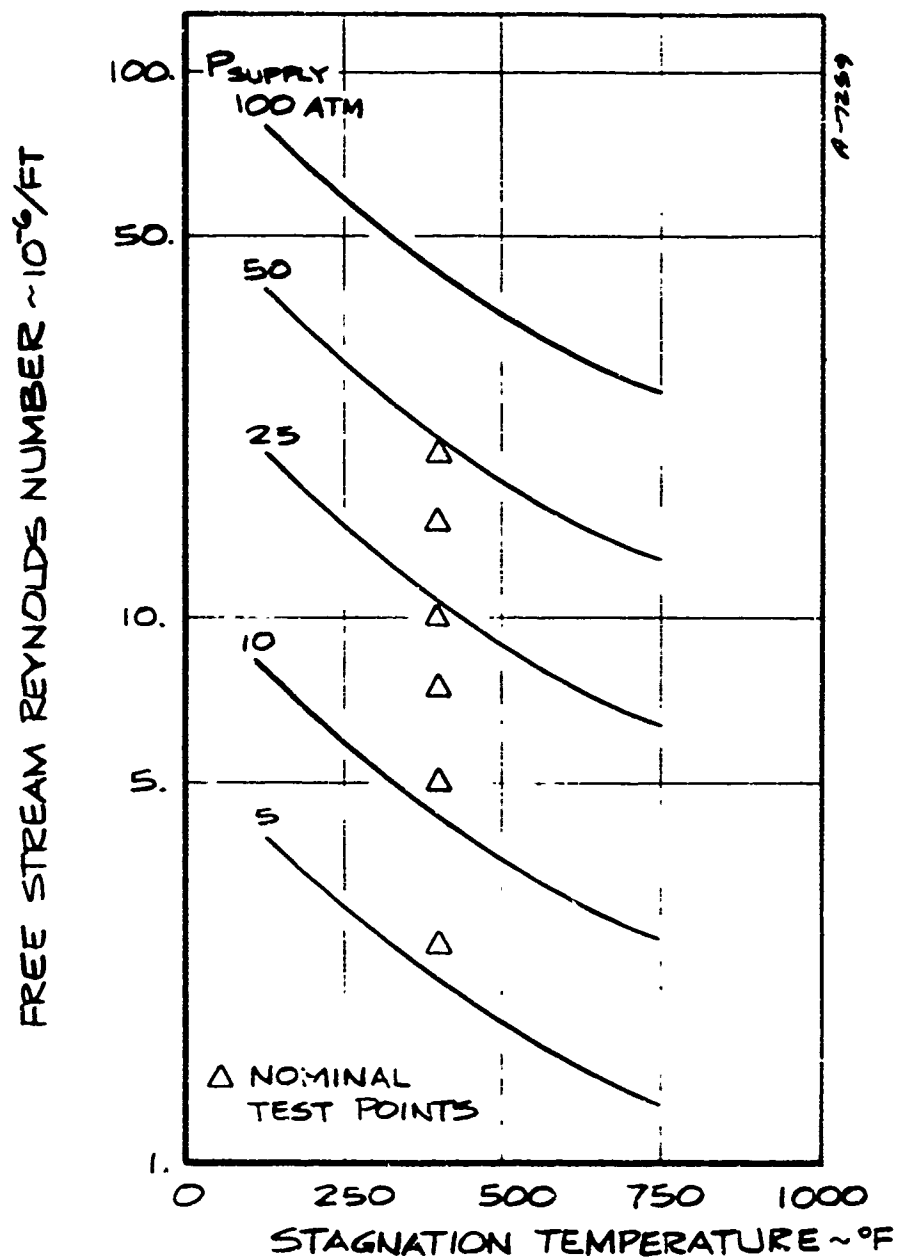


Figure 4-1. Nominal Test Points at $M_\infty = 5.0$ in NOL Hypersonic Wind Tunnel

TABLE 4-1
TEST CONDITIONS FOR PANT SERIES H WIND
TUNNEL TESTS - FEBRUARY 1974^a

Run ^b No.	Air Supply		Free Stream		Exposure Time (sec)
	P ₀ (psia)	T ₀ (°F)	M _∞	Re _∞ (10 ⁶ /ft)	
501	85	392	4.95	2.61	45.7
502	370	384	4.99	10.93	14.1
503	170	375	4.97	5.16	18.5
504	258	379	4.98	7.74	15.3
505	369	345	4.99	11.76	13.7
506	675	352	5.00	21.15	12.1
507	503	350	5.00	15.78	12.0

^aA single calorimeter was tested which was a replica of PANT, Series D, low temperature ablator, Run 201, Final Shape.

^bAll runs at zero angle of attack.

SECTION 5

DESCRIPTION OF RECORDED DATA

The primary reduced data from the Series H wind tunnel tests were heat flux distributions calculated from the recorded thermocouple data for the calorimeter model. The primary data recorded for each calorimeter run were:

- Temperature as a function of time for all thermocouples.
- Test section supply temperature and pressure as a function of time.
- Sting (or model) position as a function of time.
- Approximately 2 shadowgraph pictures.

The secondary data recorded were quick-look data which included:

- Graphical display of average thermocouple emf as a function of time for four selected channels.
- Digital display of thermocouple emf output as a function of time for four selected channels.

The paragraphs below briefly describe the primary recorded data.

At the NOL wind tunnel test facility, a 14-channel digital recorder is used for recording the test time, the supply pressure, the supply temperature, and the thermocouple temperatures. This recorder has a sampling (or sweep) rate of 0.056 second (i.e., all channels are recorded every 0.056 second). Of the fourteen channels, only thirteen are available for recording the above data. The test time, supply temperature, and supply pressure are each recorded on a separate channel, leaving 10 channels for recording temperature responses of the thermocouples. These 10 channels were multiplexed such that data from each thermocouple were sampled at least every 0.112 seconds.

Samples of typical thermocouple data are shown in Figure 5-1 as plots of temperature vs. time. A discussion of data curve fitting technique and quality is given in the data reduction section (Section 6). The thermocouple data shown in Figure 5-1 are samples from Run 502. This test was conducted at the nominal baseline Reynolds number condition ($Re_{\infty} = 10.93 \times 10^6$ ft). The figure shows example traces for each ring.

Shadowgraph photographs were taken in order to define the shock shape

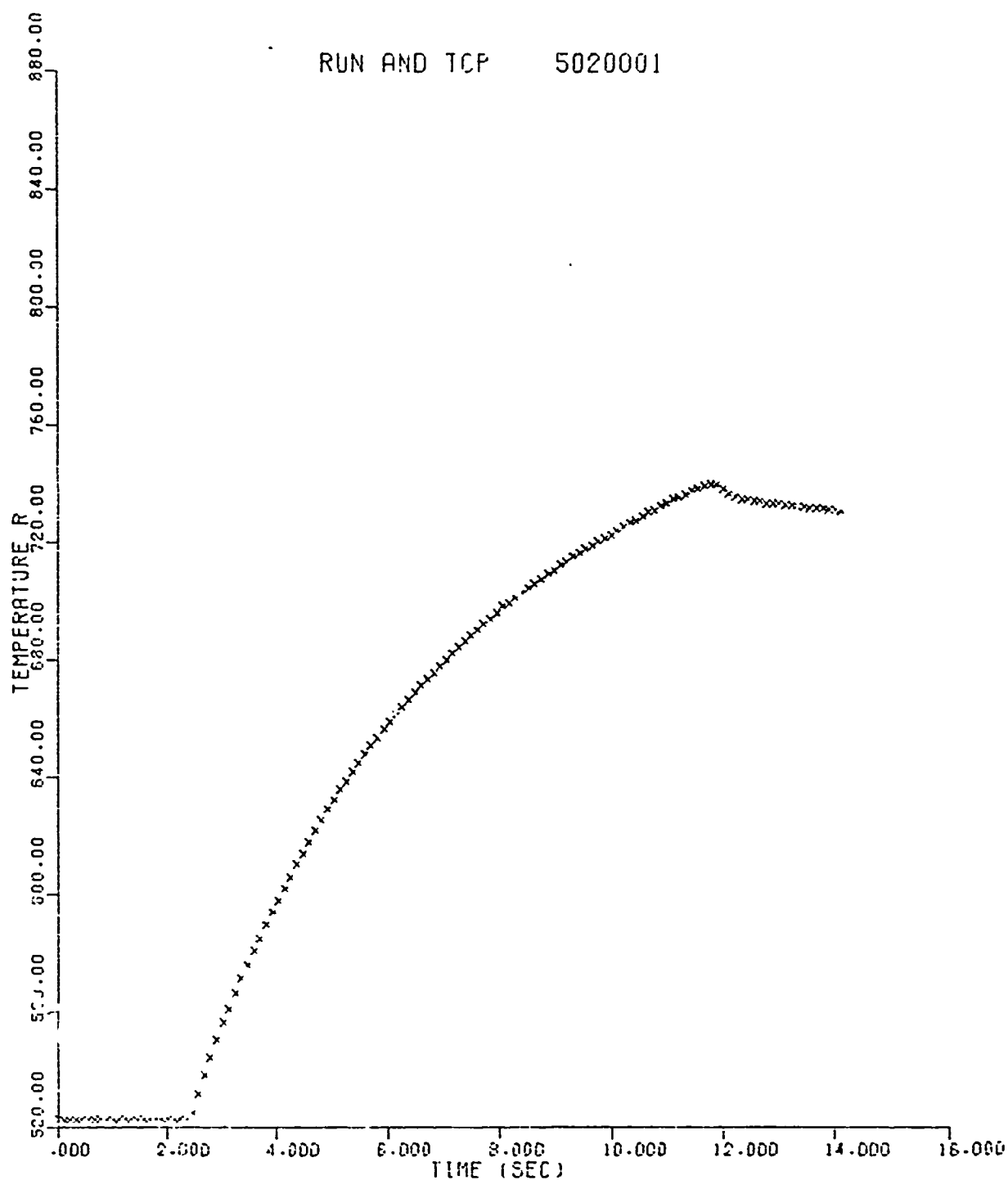


Figure 5-1. Sample of Measured Thermocouple Histories
a. Run No. 502, Thermocouple 1, Ring 1 (Nose Cap)

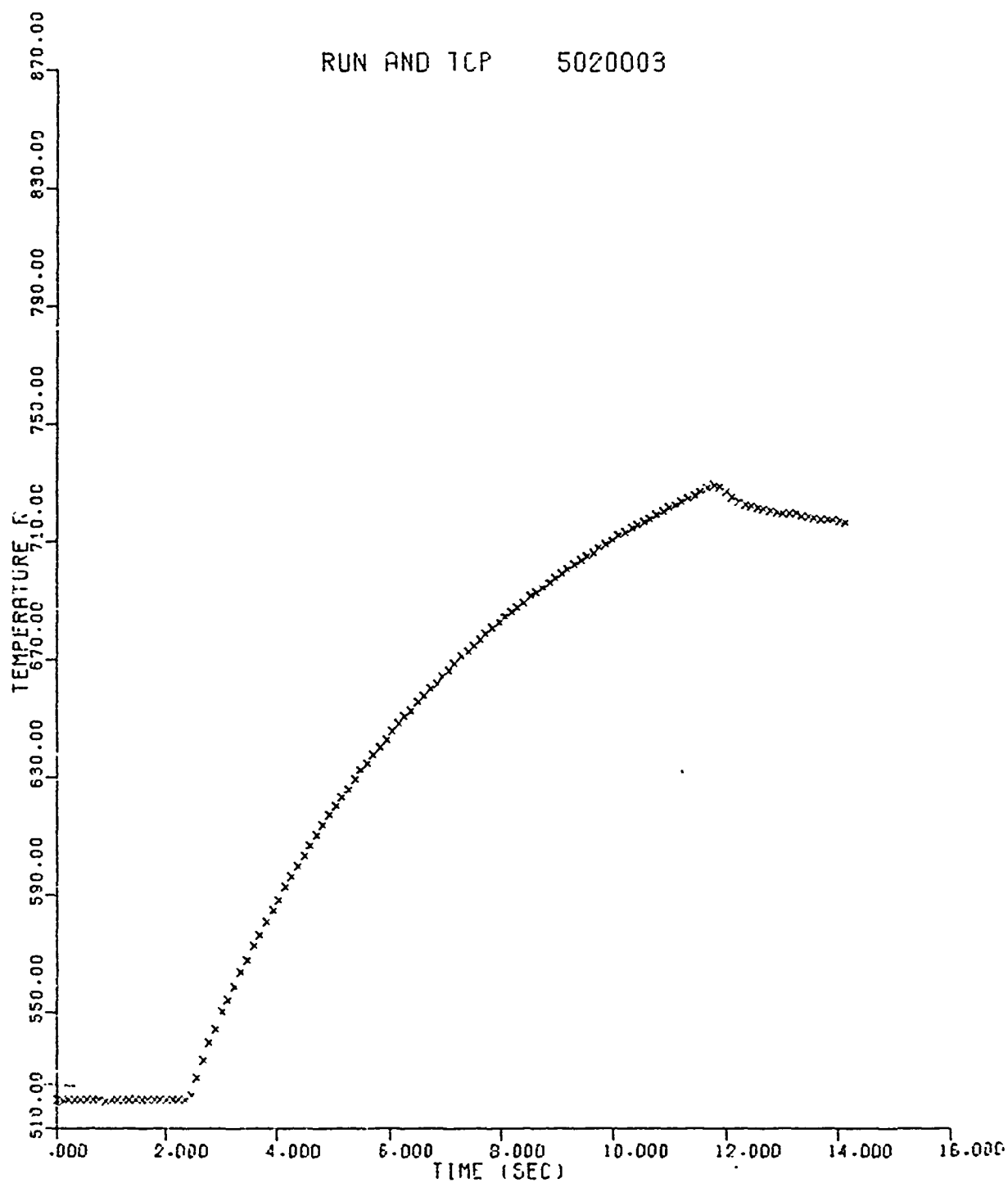


Figure 5-1. Continued

b. Run 502, Thermocouple 3, Ring 2

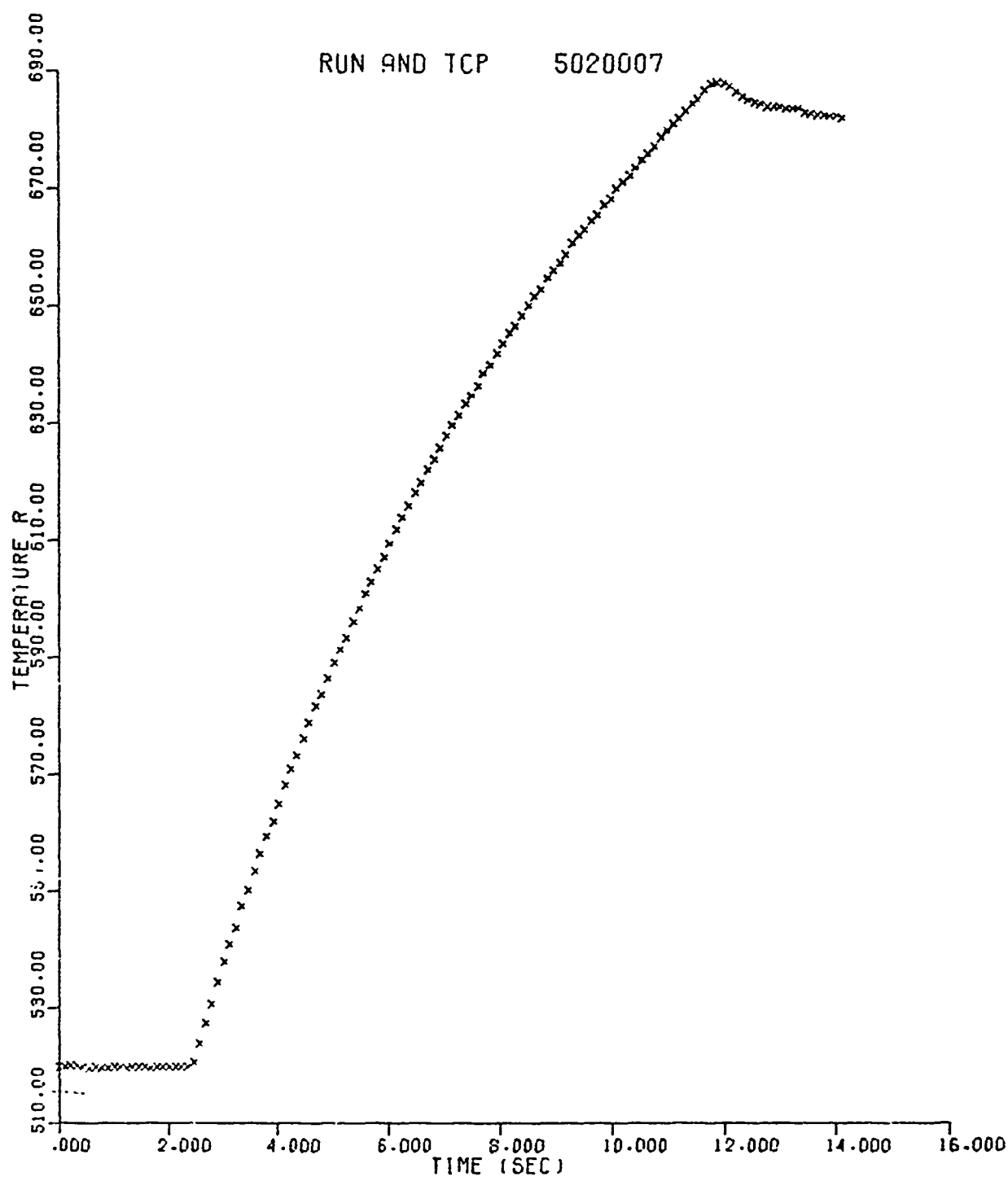


Figure 5-1. Continued

c. Run No. 502, Thermocouple 7, Ring 3

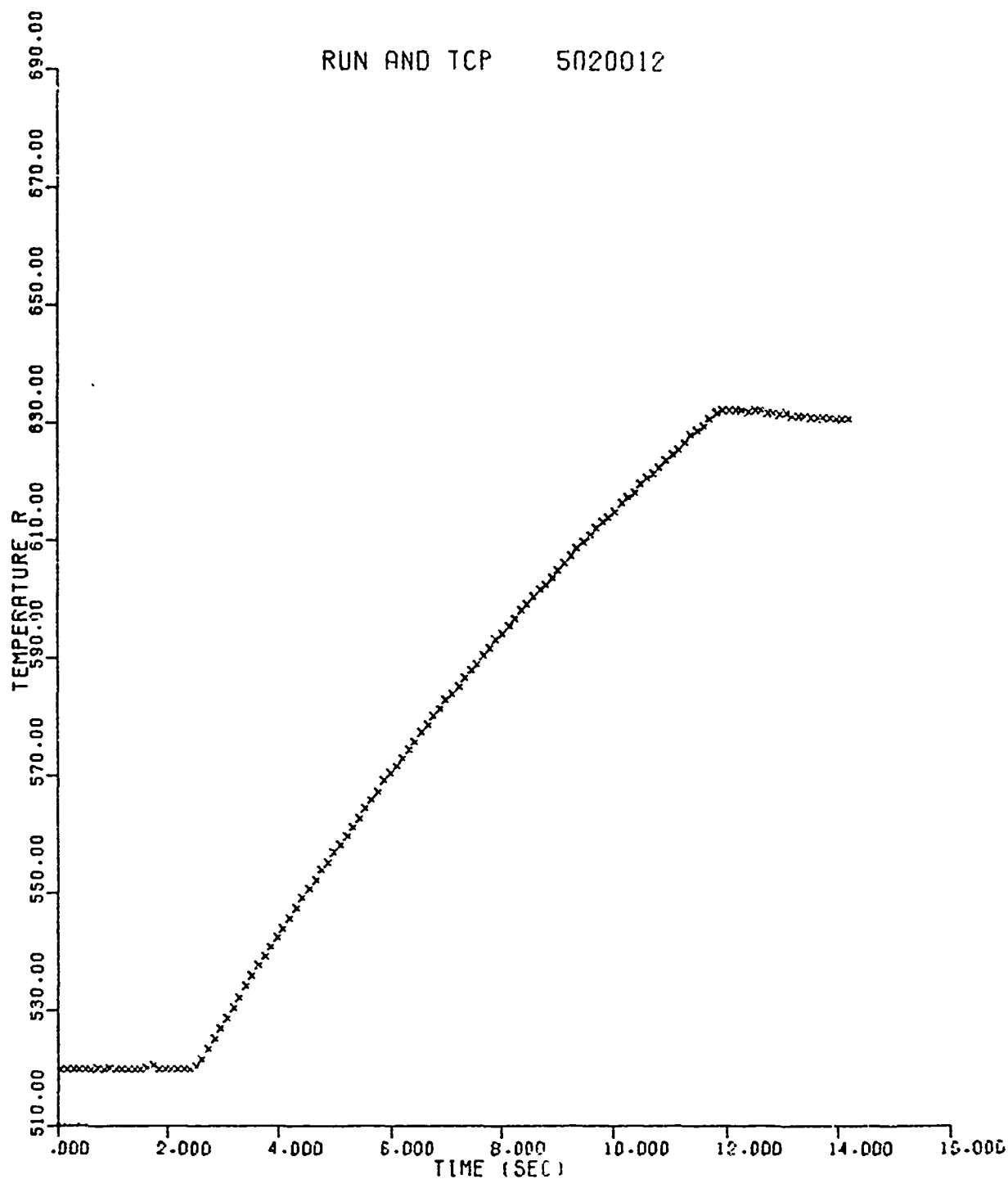


Figure 5-1. Continued

d. Run No. 502, Therocouple 12, Ring 4

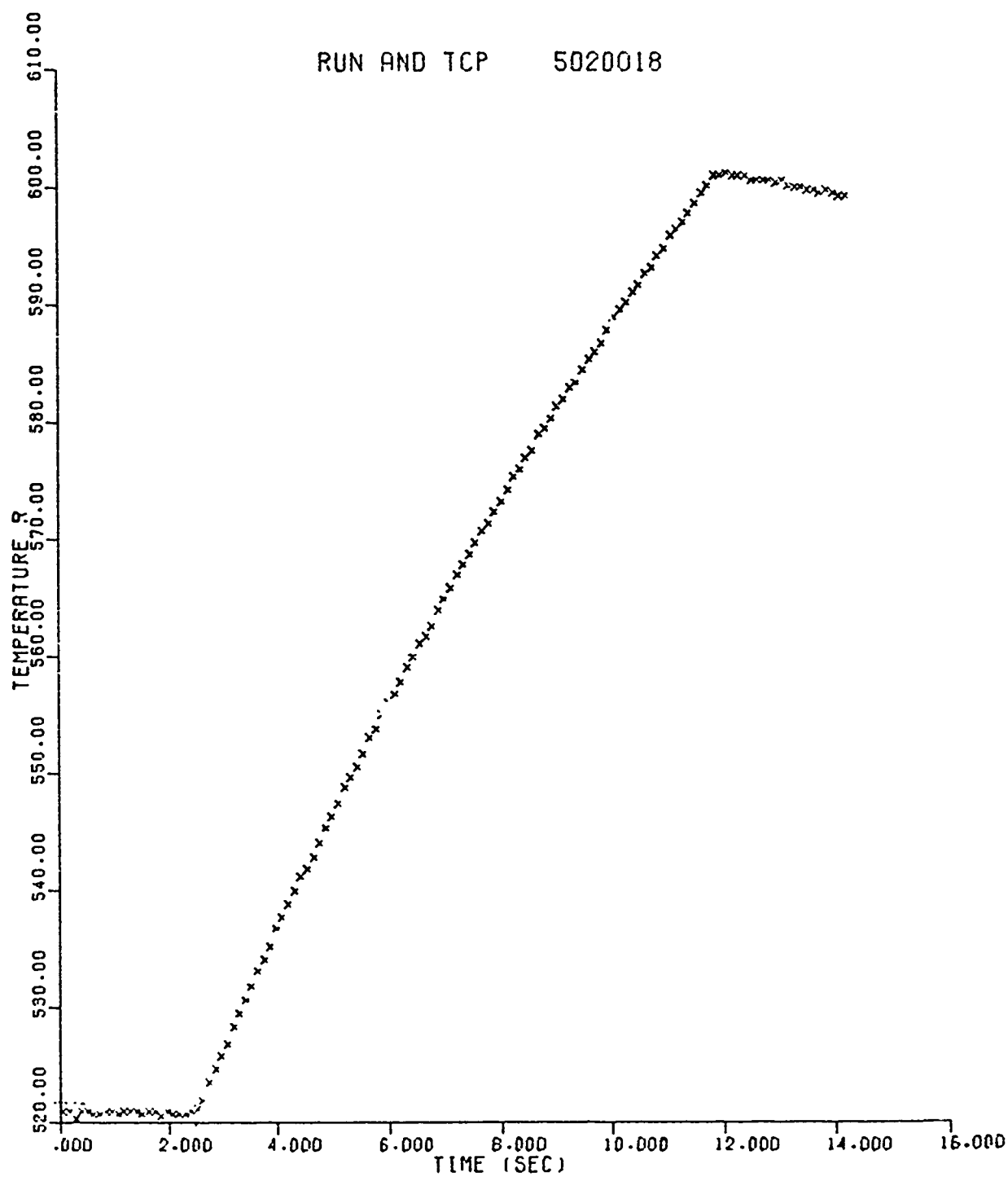


Figure 5-1. Concluded

e. Run No. 502, Thermocouple 18, Ring 5

and to determine whether any flow anomalies were occurring. Pictures were obtained by using an off axis "Z" Schlieren system (Reference 3), a spark light source, and 70 mm film. One of two types of photographs were taken, either a close-up or an overview. A sample of each type of photograph is shown in Figure 5-2.



a. Overview, Run 507



b. Close-up, Run 502

Figure 5-2. Sample Shadowgraph Photographs

SECTION 6

TEST RESULTS

The experimental data recorded during the Series H tests provide the basis for satisfying the test objectives. However, the determination of whether or not the test objectives have been satisfied can be made only after the experimental data have been reduced and analyzed. This section presents the reduced data and comparison between these data and analytical predictions. Section 6.1 briefly reviews the analysis used in obtaining calorimeter heat fluxes and calorimeter heat transfer coefficients from the measured temperature data. Section 6.2 illustrates the data reduction procedure, and Section 6.3 presents incident heat flux and heat transfer coefficients for the scallop calorimeter model.

6.1 DEFINITION OF CALORIMETER HEAT FLUX AND HEAT TRANSFER COEFFICIENT

The purpose of the calorimeter experiments is to determine convective surface heat flux (\dot{q}_{conv}) to the replicated scalloped surfaces. The principle test measurement is the temperature histories of the thermal capacitance elements (i.e., the aluminum segments). The various transient heat transfer events occurring in the calorimeter must be properly accounted for in order to relate temperature data to heat transfer rates. For example, heat conduction interactions with the HP550 epoxy and the supporting RTV must be considered. The following paragraphs describe the modeling of the calorimeter thermal system and the analyses that were performed to produce a practical data reduction technique.

A schematic of a typical aluminum/epoxy/RTV intersection is presented in Figure 6-1. Based on a control volume surrounding the aluminum segment, conservation of energy gives

$$L\dot{q}_{\text{conv}} - 2(t - t_{\text{TP}})\dot{q}_{\text{epoxy out}} + 2t_{\text{TP}}\dot{q}_{\text{epoxy in}} - L\dot{q}_{\text{RTV}} = \rho C t L \frac{dT}{d\theta} \quad (6-1)$$

where

L = width of aluminum ring

t = thickness of aluminum ring

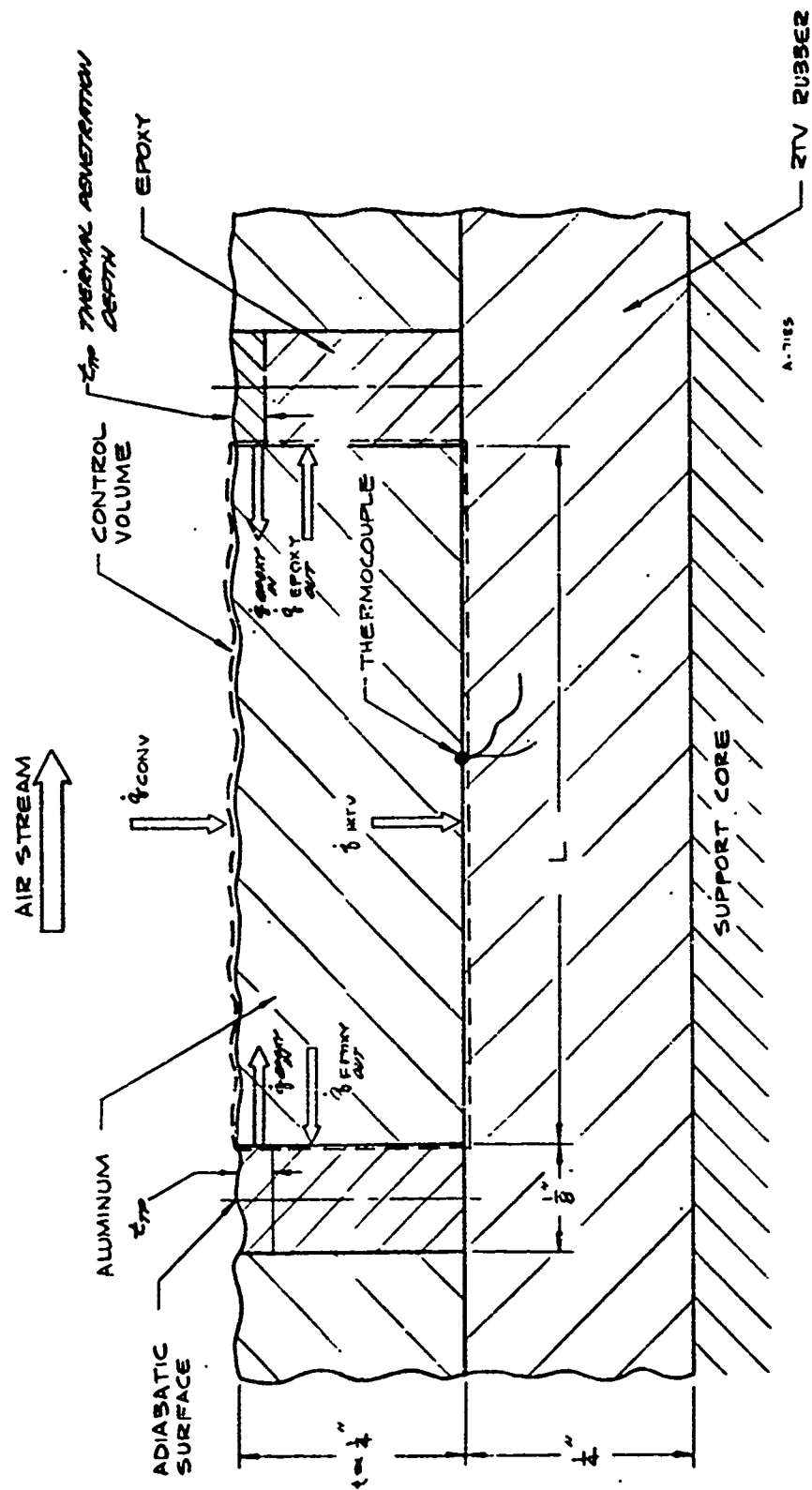


Figure 6-1. Cross-section Schematic of Typical Aluminum/Epoxy/RTV Interaction

t_{TP} = thermal penetration depth at which aluminum and epoxy temperatures are equal

ρ = density of aluminum

θ = time

\dot{q}_{conv} = convective heat flux at the air/aluminum interface

\dot{q}_{RTV} = conducted heat flux at the RTV/aluminum interface

$\dot{q}_{epoxy, out}$ = conducted heat flux flowing from aluminum to epoxy

$\dot{q}_{epoxy, in}$ = conducted heat flux flowing from epoxy to aluminum

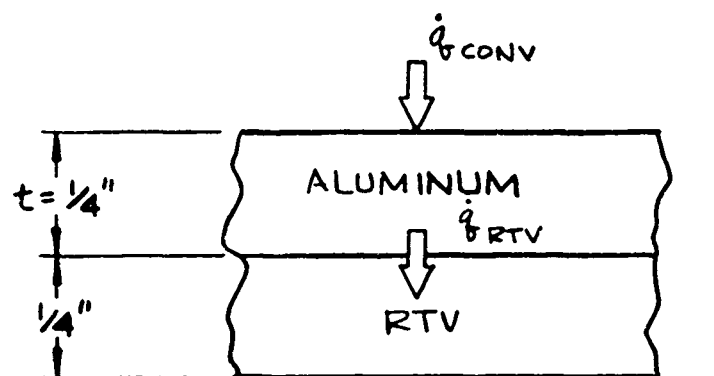
Fluxes due to radiation and loss down the thermocouple wires are dismissed as being negligible. If the net conduction heat loss is small, the convective heat flux can be evaluated directly from the measured temperature history using the approximation

$$\dot{q}_{conv} \approx \rho C t \frac{dT}{d\theta} \quad (6-2)$$

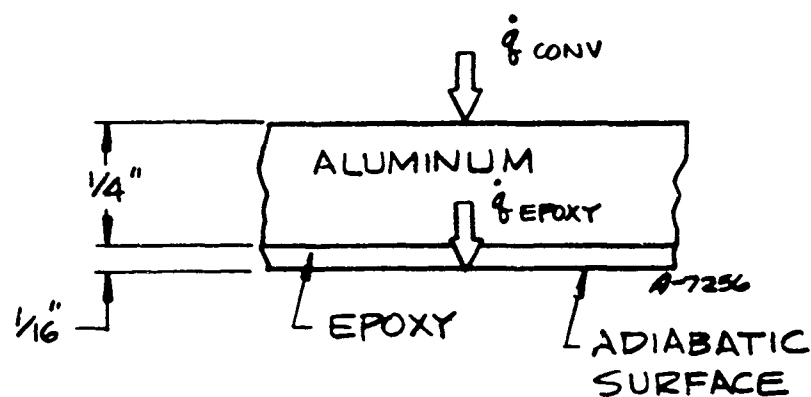
with $cT/d\theta$ determined from the measured temperature history.

The objective of the following analysis is to determine the relationship between convected and conducted heat transfer rates so that the applicability of Equation (6-2) can be assessed. To accomplish this objective, the CMA computer code was used (Reference 4). This code computes the transient thermal response of a one-dimensional multi-material system. Figure 6-2 indicates schematically the computer models used to calculate the conduction terms. Application of the CMA code to the aluminum/RTV interface is straightforward as indicated in Figure 6-2a. The required input are the material thermal properties and the convective heat transfer coefficient (h). The code calculates the temperature response of the system and the associated heat fluxes \dot{q}_{conv} and \dot{q}_{RTV} as a function of time.

The conduction fluxes at the aluminum/epoxy interface are more complicated. Since the epoxy is being convectively heated at the air/epoxy interface the "upper" portion of the epoxy is hotter than the aluminum and heat flows from epoxy to aluminum ($\dot{q}_{epoxy, in}$). However since there is such a large difference between the thermal diffusivity of aluminum and epoxy, the aluminum responds as a lumped mass and hence over the "lower" portion of the aluminum/epoxy interface the aluminum is hotter and heat flows from the aluminum to the epoxy ($\dot{q}_{epoxy, out}$).



A) COMPUTER MODEL OF ALUMINUM / RTV INTERFACE



B) COMPUTER MODEL OF ALUMINUM/EPOXY INTERFACE

Figure 6-2. Schematic of Computer Models Used to Represent the Aluminum/RTV and Aluminum/Epoxy Interfaces

A simple convectively heated slab analysis of the epoxy indicates that for environments and times of interest that only the upper 1/5 of the epoxy is conducting heat to the aluminum, and therefore the \dot{q}_{epoxy} , in flux was neglected. Neglecting this term yields a conservatively large estimation of the net conduction heat loss.

The computer model of the aluminum/epoxy interface shown in Figure 6-2b can be justified as follows. Since the aluminum responds as a lumped mass system the lower portion of the epoxy responds as a slab subjected to a given wall temperature boundary condition (i.e., the temperature of the aluminum lumped mass system). Symmetry arguments indicate that the center of the epoxy slab is an adiabatic surface, which in the analysis is the same as an insulated surface. Thus the computer model shown in Figure 6-2 retains all of the salient features of the actual system, namely an insulated half slab of epoxy adjacent to a convectively heated aluminum mass.

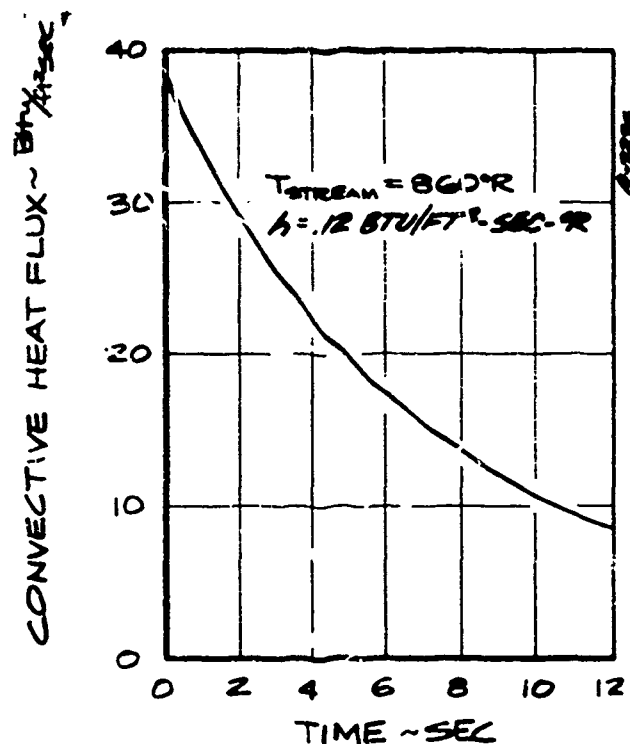
Figure 6-3 shows typical plots of calculated heat flux histories for the convective surface and the aluminum/epoxy and aluminum/RTV interfaces. The nominal thermal properties used for these calculations are given in Table 6-1

TABLE 6-1
NOMINAL THERMAL PROPERTIES FOR
CALORIMETER CALCULATIONS

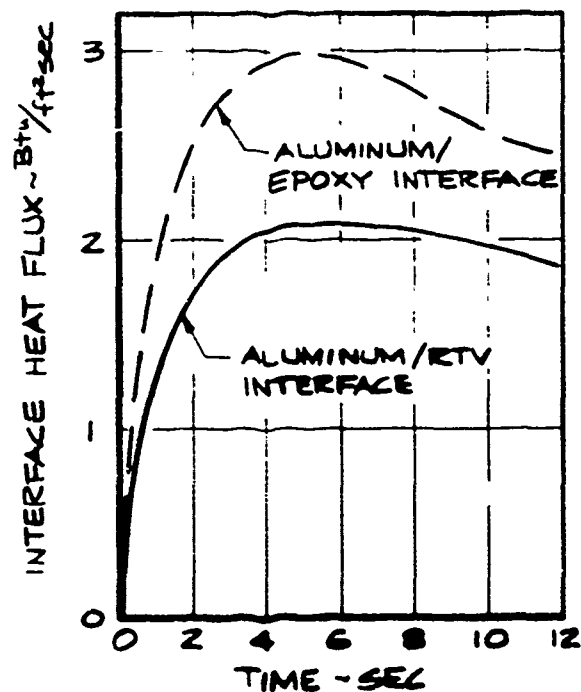
Material	Density ρ (lbm/ft ³)	Specific Heat C (Btu/lbm-°R)	Conductivity k (Btu/sec-ft-°R)	Thermal Diffusivity α (ft ² /sec)
Aluminum	169	.22	2.55×10^{-2}	6.86×10^{-4}
Epoxy	86.81	.287	5.78×10^{-5}	1.72×10^{-6}
RTV	73.13	.35	3.359×10^{-5}	1.31×10^{-6}

An analysis was performed to determine the relative values of convected and the conducted heat transfer rates. Accounting for the appropriate areas over which the different fluxes occur, the ratio of the conducted to the convected heat transfer rates is given by

$$\frac{\text{conducted rate}}{\text{convected rate}} = \frac{(2t/L) \dot{q}_{\text{epoxy}} + \dot{q}_{\text{RTV}}}{\dot{q}_{\text{conv}}} \quad (6-3)$$



A) CONVECTIVE HEAT FLUX HISTORY



B) INTERFACE HEAT FLUX HISTORIES

Figure 6-3. Typical Calculated Heat Flux Histories

where

t = aluminum thickness

L = aluminum ring width

A plot of this ratio is shown in Figure 6-4 for the calculation shown in Figure 6-3. As Figure 6-4 indicates, the ratio of the conducted to convected heat rates increases with time as the convected flux decreases while the conducted flux increases. For the conditions shown in Figure 6-4 the conducted flux is greater than 10 percent of the convective flux for times greater than approximately 1.5 seconds.

The plot shown in Figure 6-4 is for one value of heat transfer coefficient (h), ring width (L), and ring thickness (t). It is impractical to perform computer calculations for each ring for each operating condition therefore a correlation of these computer solutions is required. The appropriate correlation parameters were obtained from the closed form solution for a lumped mass exposed to a convective environment

$$\frac{T - T_{\infty}}{T_i - T_{\infty}} = e^{-\frac{h\theta}{\rho C t}} \quad (6-4)$$

where

T = instantaneous temperature of the lumped aluminum mass

T_i = initial temperature of the lumped mass

T_{∞} = environmental temperature

Therefore for a given material and environment temperature the instantaneous temperature of a lumped mass is only a function of $h\theta/t$ or

$$\tau = f\left(\frac{h\theta}{t}\right) \quad (6-5)$$

Similarly since

$$\dot{q}_{\text{conv}} = h(T_{\infty} - T) \quad (6-6)$$

CONDUCTED HEAT RATE / CONVECTED HEAT RATE

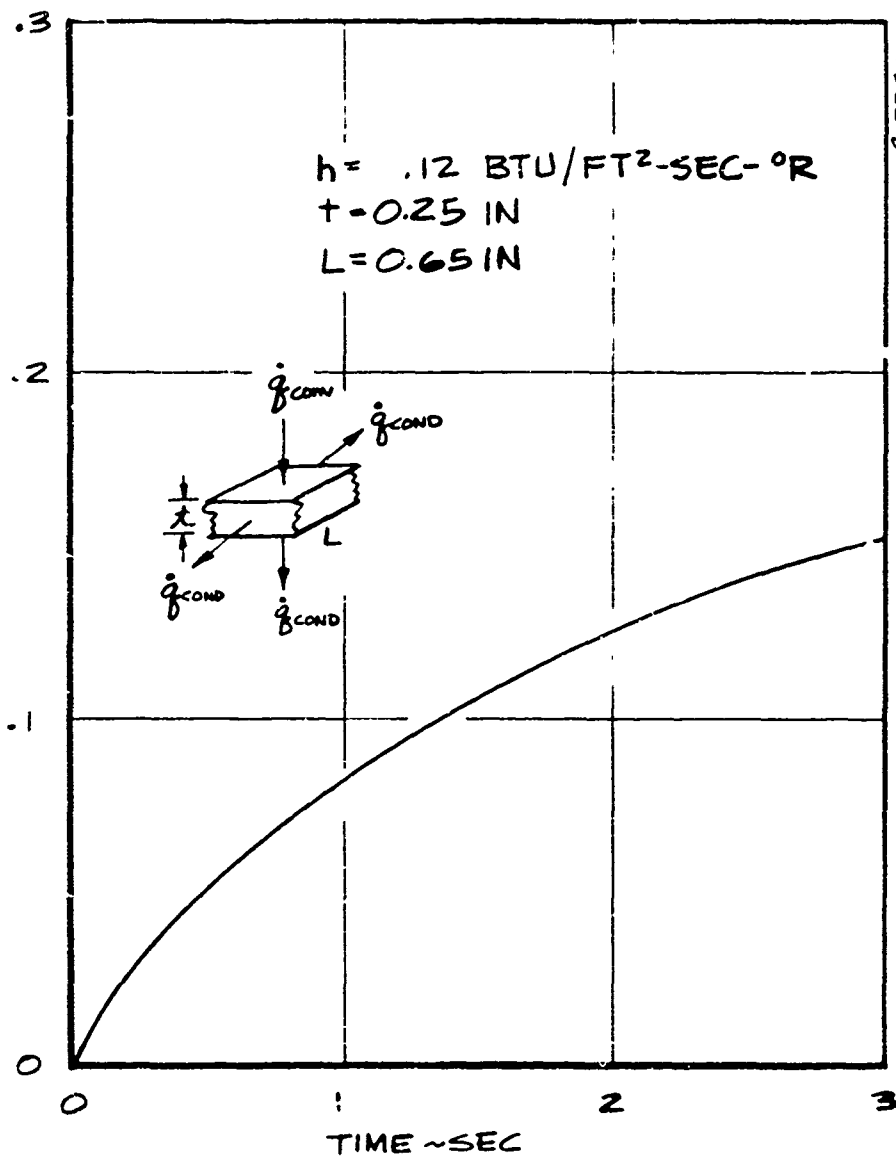


Figure 6-4. Typical Ratio of Conducted to Convected Heat Rate Versus Time

Then

$$\dot{q}_{\text{conv}} = f\left(\frac{h\theta}{t}\right) \quad (6-7)$$

As explained in the modeling description the RTV and epoxy respond as slabs subjected to a time dependent wall temperature boundary condition ($T(\theta)$). Therefore it is reasonable to anticipate that the appropriate similitude parameter for the conduction loss terms is $dT/d\theta$; from Equation 6-4

$$\frac{dT}{d\theta} = f\left(\frac{h}{t}, \frac{h\epsilon}{t}\right)$$

Figure 6-5 shows a comparison of two computer solutions for the conduction loss at the aluminum/RTV interface (\dot{q}_{RTV}) for two different values of transfer coefficient (h) and wall thickness (t) but the same ratio of h/t . The plot shows \dot{q}_{RTV} versus $h\theta/t$. Although the thicker slab shows a longer initial response time the two solutions closely approach one another. The agreement shown in Figure 6-5 demonstrates that the chosen correlation parameters are adequate.

Calculated conduction loss fluxes for both the RTV and epoxy interfaces are shown for several h/t ratios in Figure 6-6. Lines of constant time ($\theta = 1.0$ second) are also shown cross plotted on Figure 6-6. The cross plots of conduction losses at 1 second can be combined with the equation for the convective flux (Equation 6-6) and the equation for the conducted/convected ratio (Equation 6-3) to produce plots of conduction/convection versus heat transfer coefficient at time equal 1.0 second. Due to the nearly linear initial dependence of both conduction and convection terms on transfer coefficient the ratio of these quantities is initially nearly independent of transfer coefficient. Hence at the one second time the ratio of conduction to convection is independent of test condition and dependent only on ring width (L) and thickness (t). Table 6-2 gives a summary of these calculated ratios for each ring.

TABLE 6-2
CALCULATED CONDUCTION/CONVECTION RATIOS
AT TIME = 1.0 SECOND

Ring No.	t_{ave} (inches)	L (inches)	$\frac{\text{Conducted}}{\text{Convective}}$
2	.166	.555	.103
3	.226	.660	.081
4	.283	.970	.059
5	.269	1.325	.053

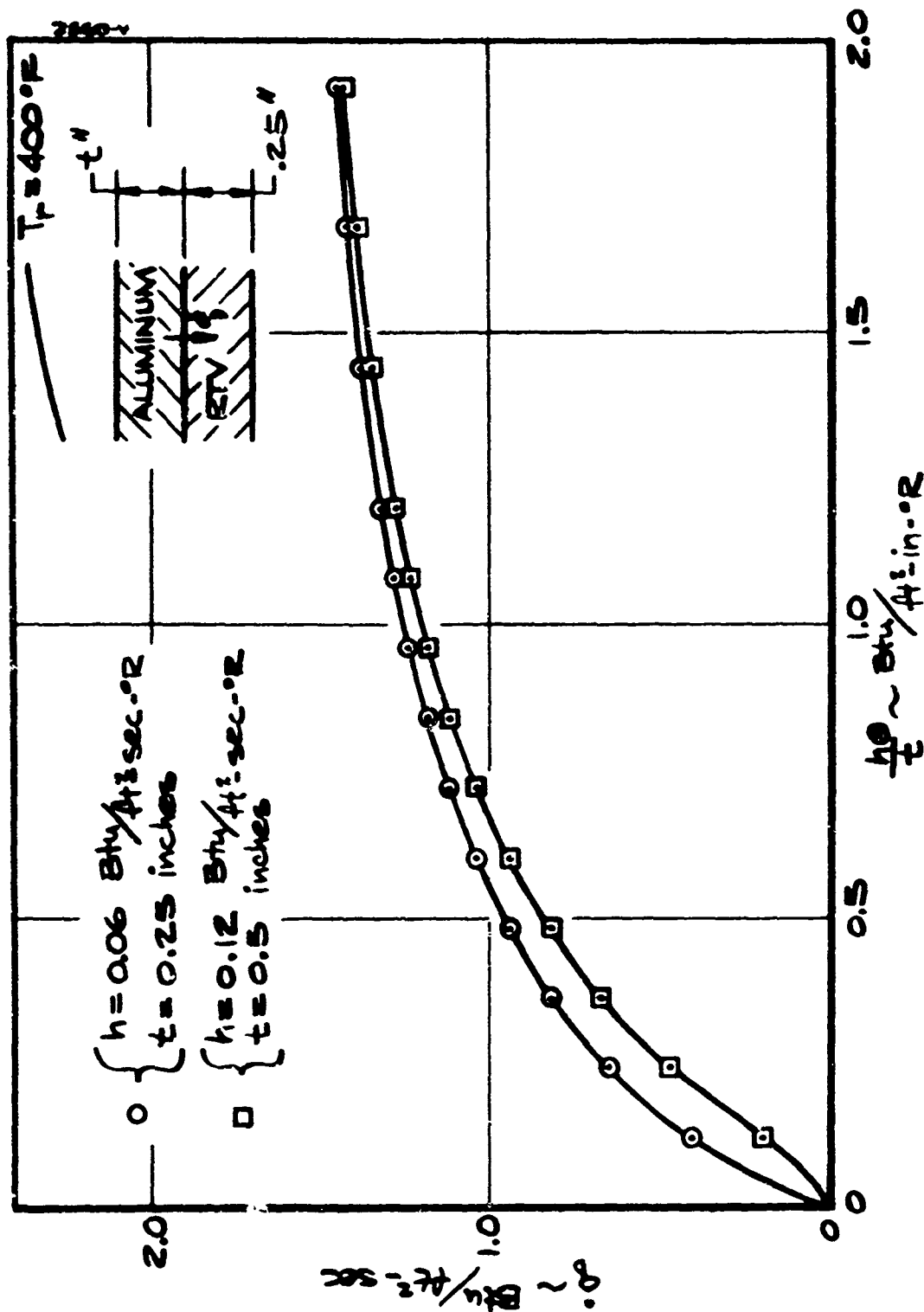


Figure 6-5. Comparison of Two Different Conduction Loss Calculations When Plotted Versus Correlation Parameters

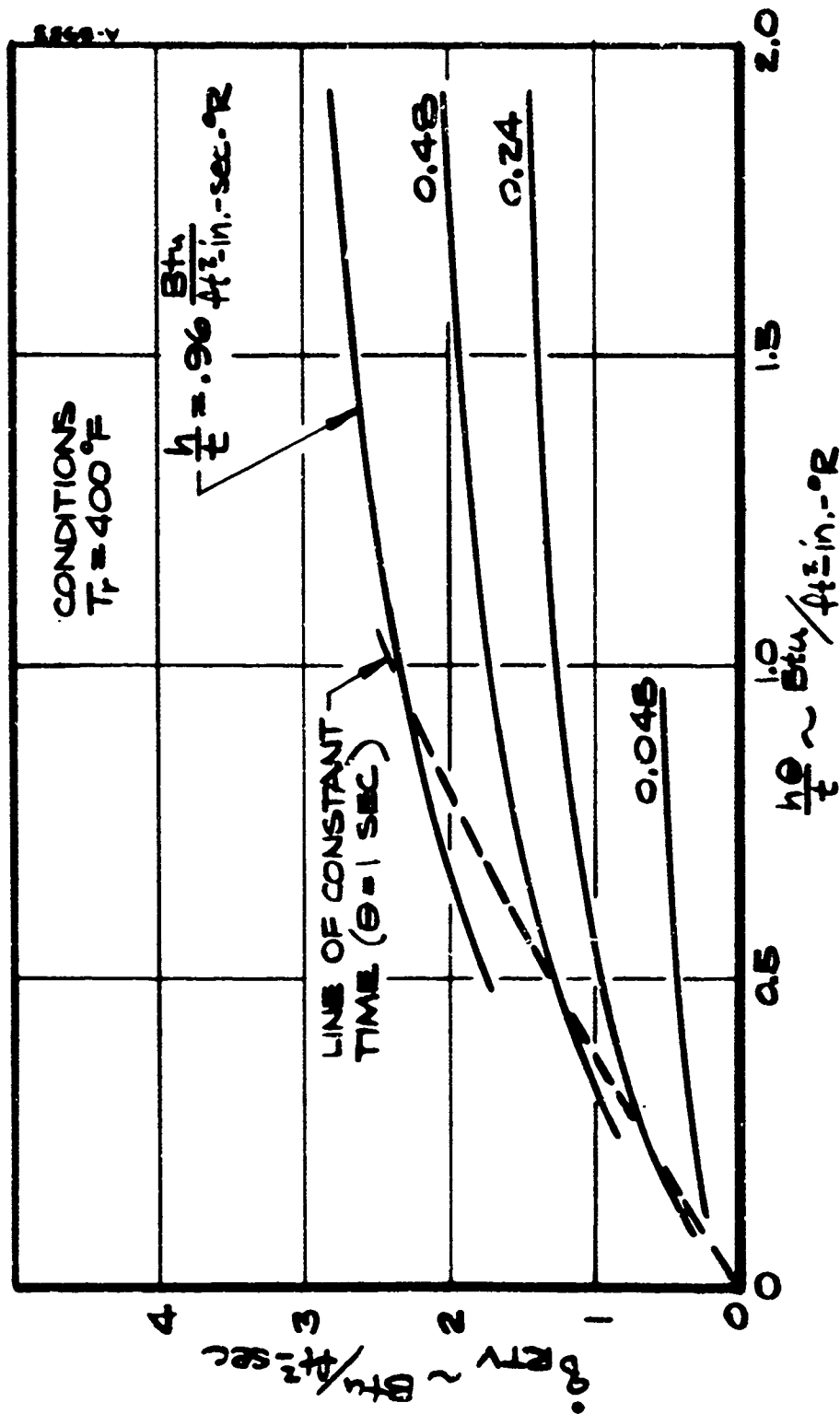


Figure 6-6. Conduction Loss Terms Plotted Versus Correlation Parameters

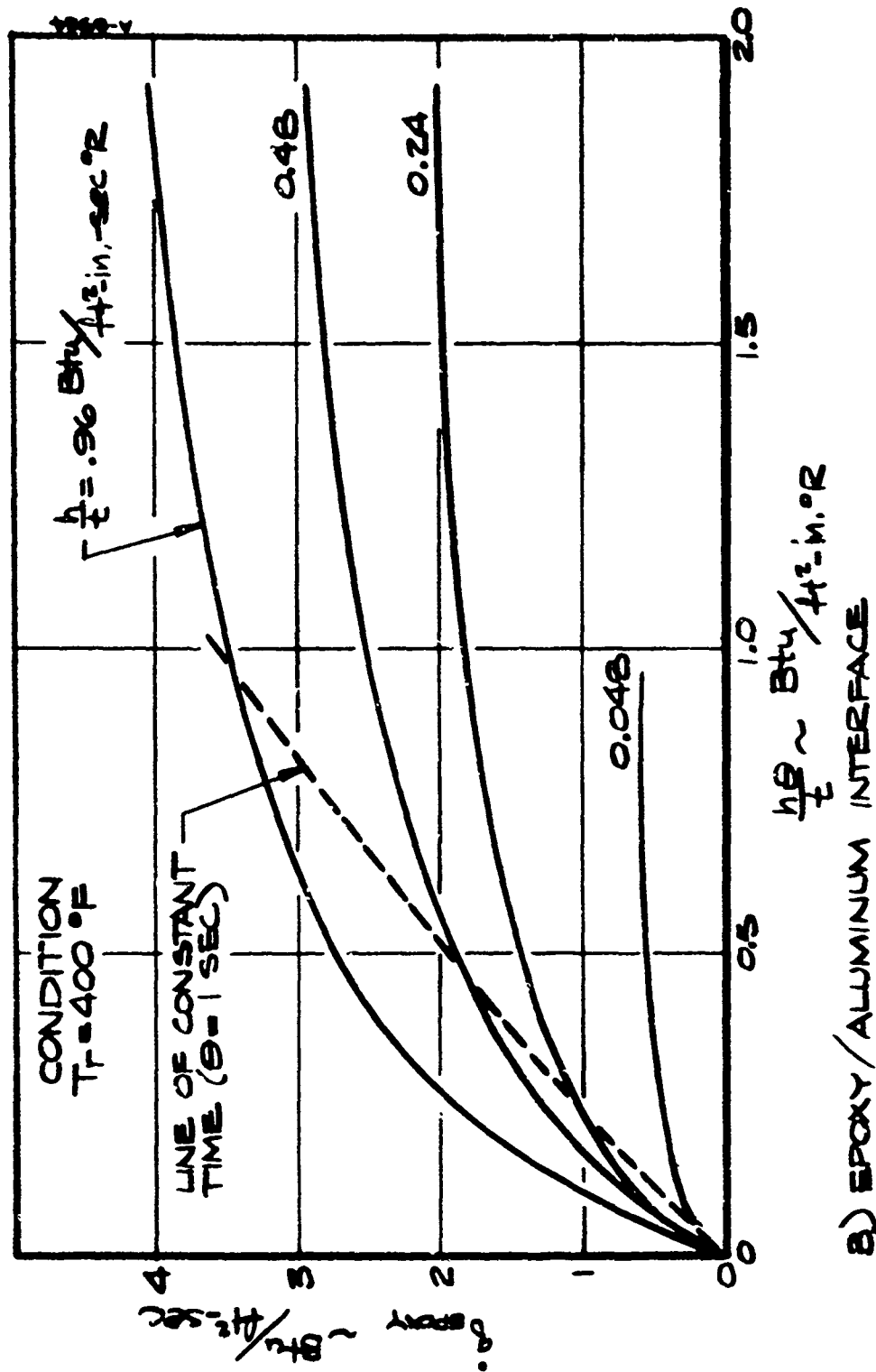


Figure 6-6. Concluded

Calculations of the conduction loss terms for the small nose cap piece were not performed because of uncertainty involved in measuring the epoxy and RTV interface areas. Also there is uncertainty in calculating the projected surface area for convective heat transfer.

The conduction/convection ratios given in Table 6-2 indicate that even for the worst case (ring 2) the error incurred by neglecting conduction terms in calculating the convective heat flux (i.e., using Equation (6-2) is no more than 10.3 percent. Furthermore the actual error is less than this since the heat conducted to the aluminum from the convectively heated epoxy ($\dot{q}_{\text{epoxy, in}}$) was not included in the calculation of the net conduction loss. It is concluded, therefore, that Equation 6-2 is sufficiently accurate for the reduction of the Series H data.

Once the incident heat flux (\dot{q}_{conv}) has been computed from Equation (6-2) the convective heat transfer coefficient can be determined from

$$h = \frac{\dot{q}_{\text{conv}}}{T_r - T_w} \quad (6-8)$$

where

h = convective heat transfer coefficient

T_r = boundary layer edge recovery temperature

T_w = wall temperature

The recovery temperature is obtained from

$$\frac{T_r}{T_o} = \frac{T_e}{T_o} + R_f \left(1 - \frac{T_e}{T_o} \right) \quad (6-9)$$

The recovery factor (R_f) was taken as $Pr^{1/3} = 0.892$ which corresponds to turbulent flow. The boundary layer edge temperature (T_e) was calculated based on real gas isentropic expansion equations using a pressure distribution computed according to the procedure described in Reference 6. The pressure distribution and corresponding recovery temperature distribution are shown in Figures 6-7 and 6-8. The shock shape used for the recovery temperature distribution calculation and all predictions which follow was measured from close-up shadow-graph photographs (Figure 5-2) and is shown plotted in Figure 6-9.

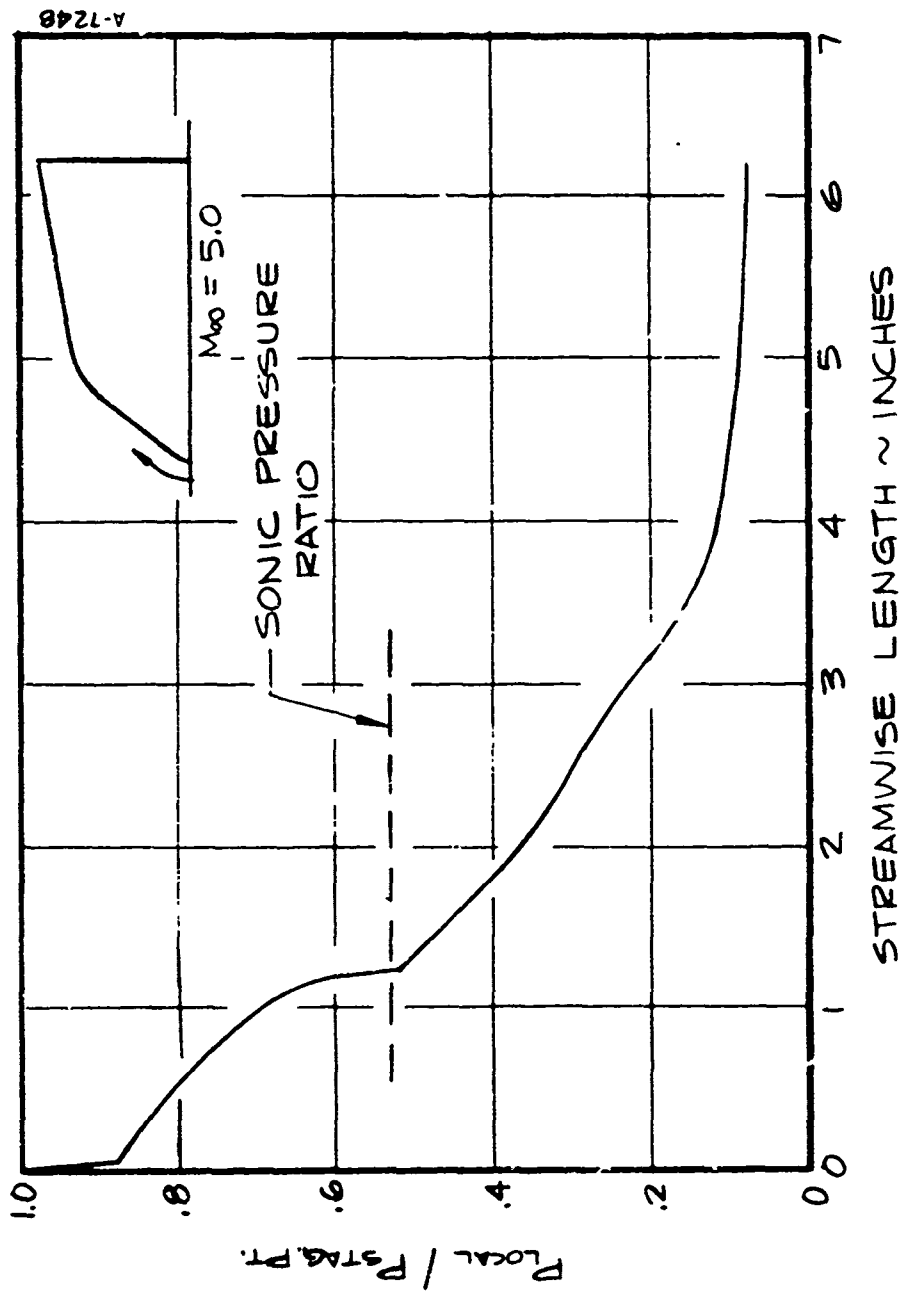


Figure 6-7. SAANT Calculation of Pressure Distribution Along Steady Shape of Run 201

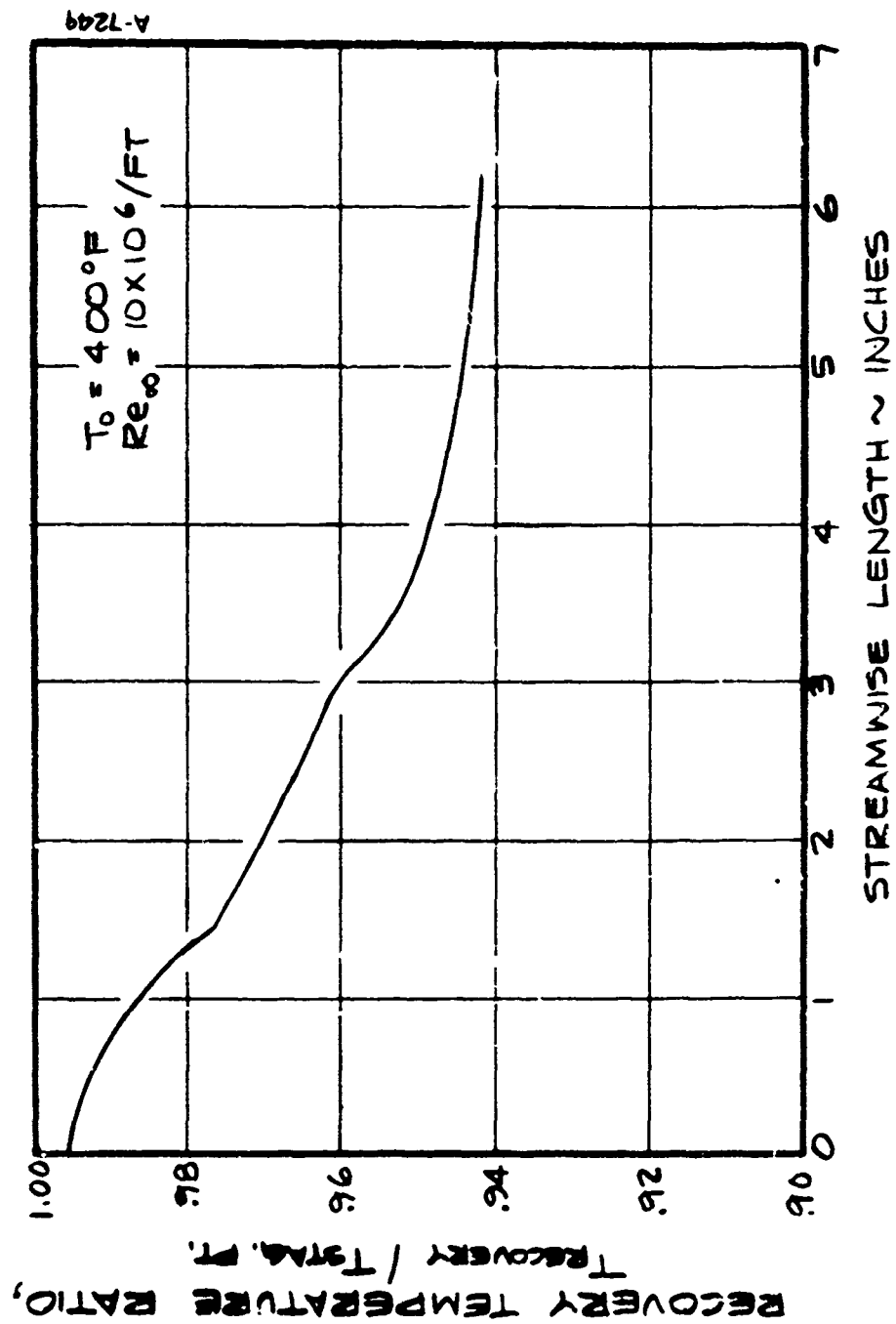


Figure 6-8. Predicted Recovery Temperature Distribution Along Steady Shape of Run 201

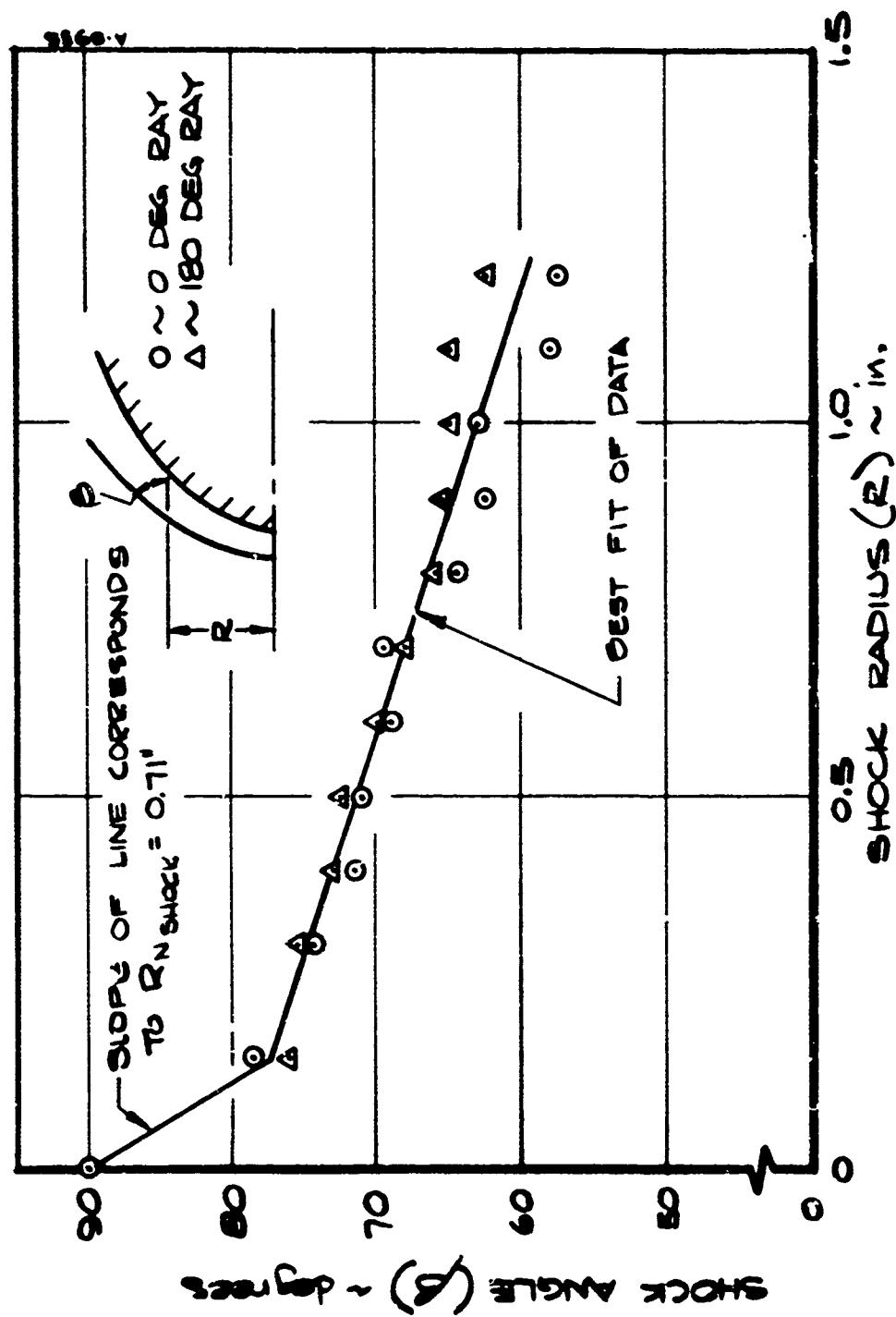


Figure 6-9. Measured Shock Shape for Run 502 ($Re_\infty = 10.93 \times 10^5/\text{ft}$, $M_\infty = 5$)

Due to the small effect of shock shape on recovery temperature (less than 0.5 percent) and based on Figure 6-9 the 70° oblique shock recovery temperature distribution was used in all data reduction.

6.2 DATA REDUCTION

Calculating the incident heat flux from Equation (6-2) requires knowing the slope of the temperature history. Because of the significance at early times of small temperature variations on the temperature slope and, thus, on the calculated incident heat flux, the measured temperatures were curve fit prior to defining the slope. This calculation was performed using the splined quadratic least squares curve fit technique described in Appendix A of Reference 5. Each quadratic was least squares fit to six data points and a total of four splined quadratic curves were used for each thermocouple temperature history. The thermocouple temperature data for these calculations were obtained from magnetic tapes which were forwarded to Aerotherm from NOL. In addition, NOL personnel transmitted computer listings of measured temperatures and free stream environmental conditions and computer plots of time-temperature data for all thermocouples. These plots served two purposes: 1) they provided a check of the data written on magnetic tapes, and 2) they provided the basis for identifying abnormal data.

The heat flux distributions along the model surface were calculated from the curve-fitted temperature data using Equation (6-2). The time-temperature slopes for all thermocouples were evaluated at 1.0 second after the first response of the nose cap thermocouple (T.C.#1). The average effective wall thickness for each ring was defined in Section 3.2 and the calorimeter thermal properties were given in Section 3.3.

6.3 HEAT FLUX AND HEAT TRANSFER COEFFICIENT DISTRIBUTIONS

Heat flux and heat transfer coefficient values were calculated for all thermocouples using the technique described in Section 6.2. During the course of this data reduction it was noted that certain thermocouples were found to give consistently suspicious results. Figure 6-10 shows comparisons of fitted temperature/time slope ($dt/d\theta$) versus time for a typical thermocouple and a suspicious thermocouple. The anticipated thermocouple response is for $dT/d\theta$ to monotonically decrease since convective heat transfer to a segment will decrease with increasing wall temperature and conduction losses will increase with increasing segment temperature. The response of the suspicious thermocouple may be indicating a poor thermal attachment because the response time

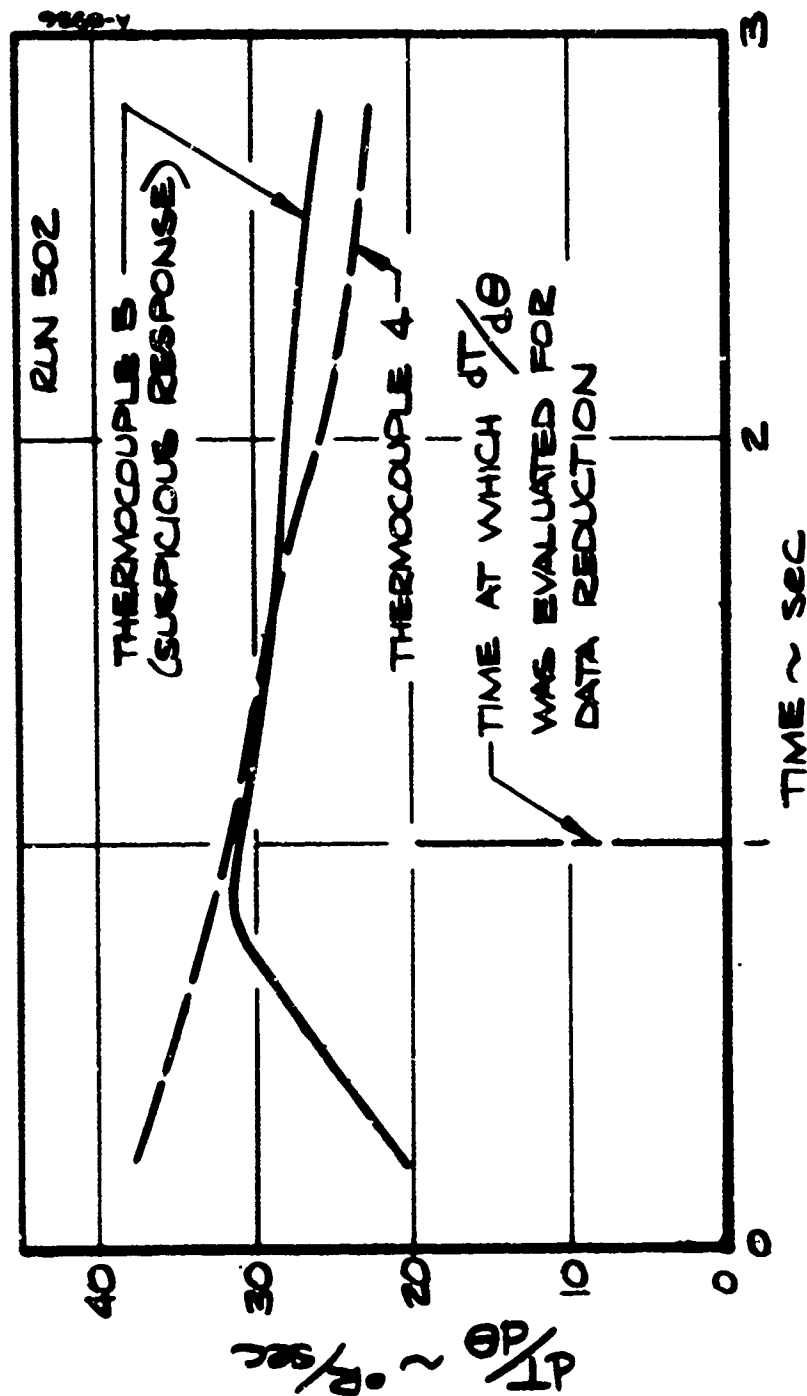


Figure 6-10. Comparison of Typical Thermocouple Response to Suspicious Thermocouple Response

is increased. It is possible, however, that the suspicious trend is a result of local differences in segment thickness which damp out after the initial transient.

Reduced heat flux data are shown plotted versus streamwise length (S) for each meridional location in Figure 6-11. All data reduction was performed for a test time of 1.0 second and, therefore, the local wall temperature is a function of body location and test conditions. For the baseline test (Run 502) the wall temperature of the forecone (Ring 2) is approximately 580°R at 1.0 second and the aftcone (Ring 5) is about 535°R. Consistently suspicious thermocouples are indicated by flagged symbols.

Distributions of reduced heat transfer coefficient data are shown in Figure 6-12. Also shown are SAANT Computer Code (Reference 6) smooth wall transfer coefficient predictions. The upper line in each case is the prediction for a fully turbulent boundary layer and the lower line corresponds to a laminar boundary layer. The shock shape used for the SAANT code predictions was determined from shadowgraph photograph measurements (Figure 6-9). Even with the high quality close-up Schlieren photographs available the measurement of the shock radius of curvature at the stagnation point is still uncertain; a nominal radius of 0.71 inch was used for the code predictions. Reference 7 presents parametric calculations showing the effect of shock curvature on predicted heat transfer coefficient distribution. The calculations shown in Reference 7 indicate that the smaller the shock radius the closer the heating increase caused by swallowing the oblique shock streamlines is to the stagnation point. For the nominal shock radius used in the predictions (i.e., 0.71 in.) the onset of oblique shock cone entropy occurs at a streamlength of about 1.0 inch.

It should be noted that for both the heat flux and the heat transfer coefficient plots the reduced data for the thermocouples on a given ring are consistently ordered from run to run. For instance on ring number three the 0 degree ray is always high, followed by the 90 degree ray and the 180 degree is always the lowest. This type of consistent ordering indicates that the effective wall thicknesses in the vicinity of the thermocouples are different than the average. In order to eliminate this systematic uncertainty the calorimeter would have to be sectioned to obtain local thickness. This has not been done. A duplicate casting was made during model fabrication to resolve such questions, but section thicknesses of the two castings could not be made exactly the same.

Comparisons between smoothwall turbulent predictions and the data are generally as anticipated. That is, heat transfer to the scalloped surface is higher than smoothwall heat transfer.

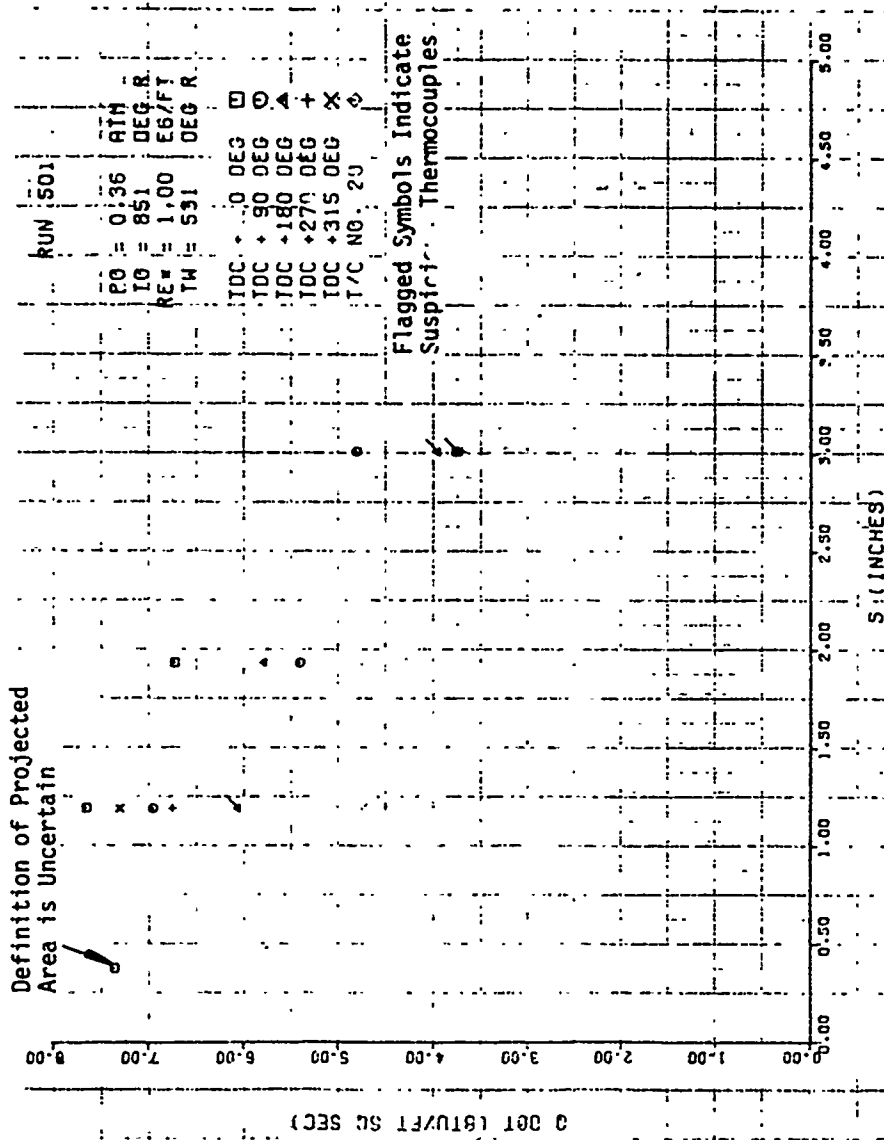


Figure 6-11. Incident Heat Flux Distribution, Scallop Calorimeter Model

a. Run 501 ($Re_{\infty} = 2.61 \times 10^6/ft$)

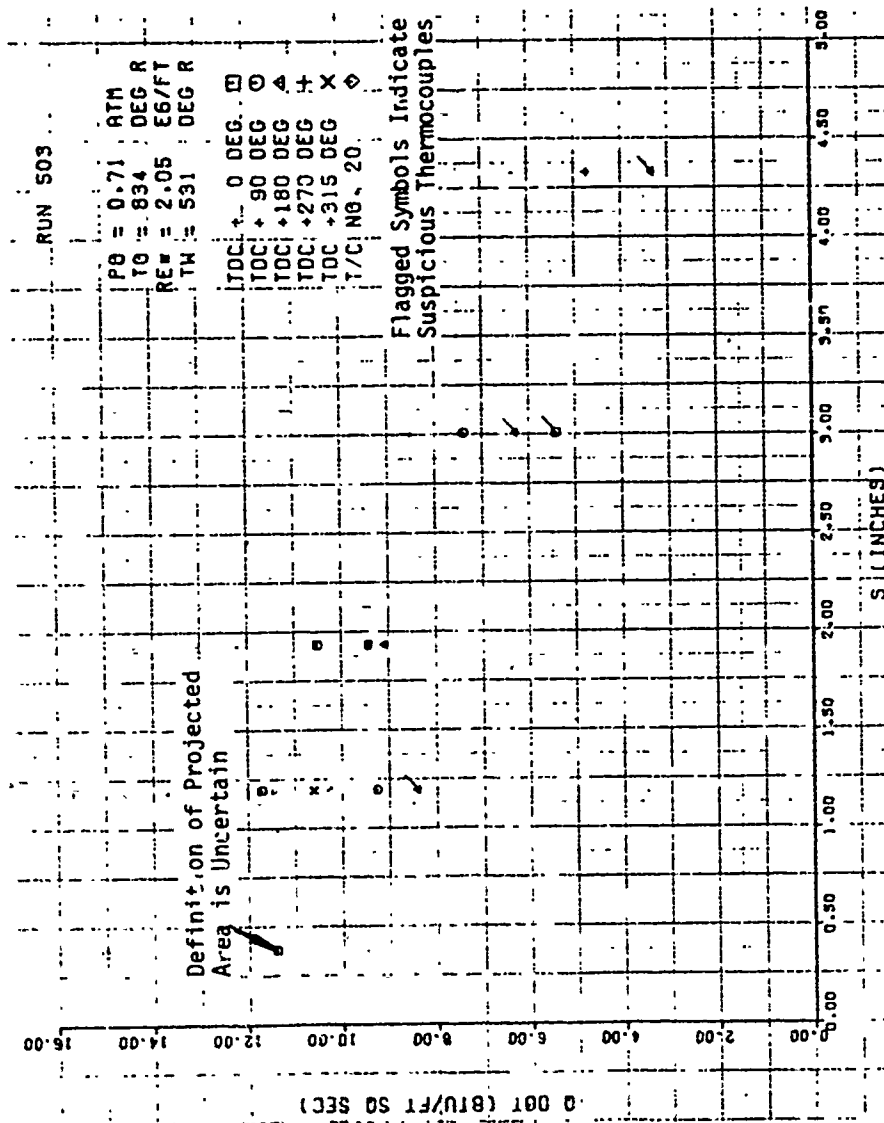


Figure 6-11. Continued

c. Run 503 ($Re_{\infty} = 5.16 \times 10^6 / ft$)

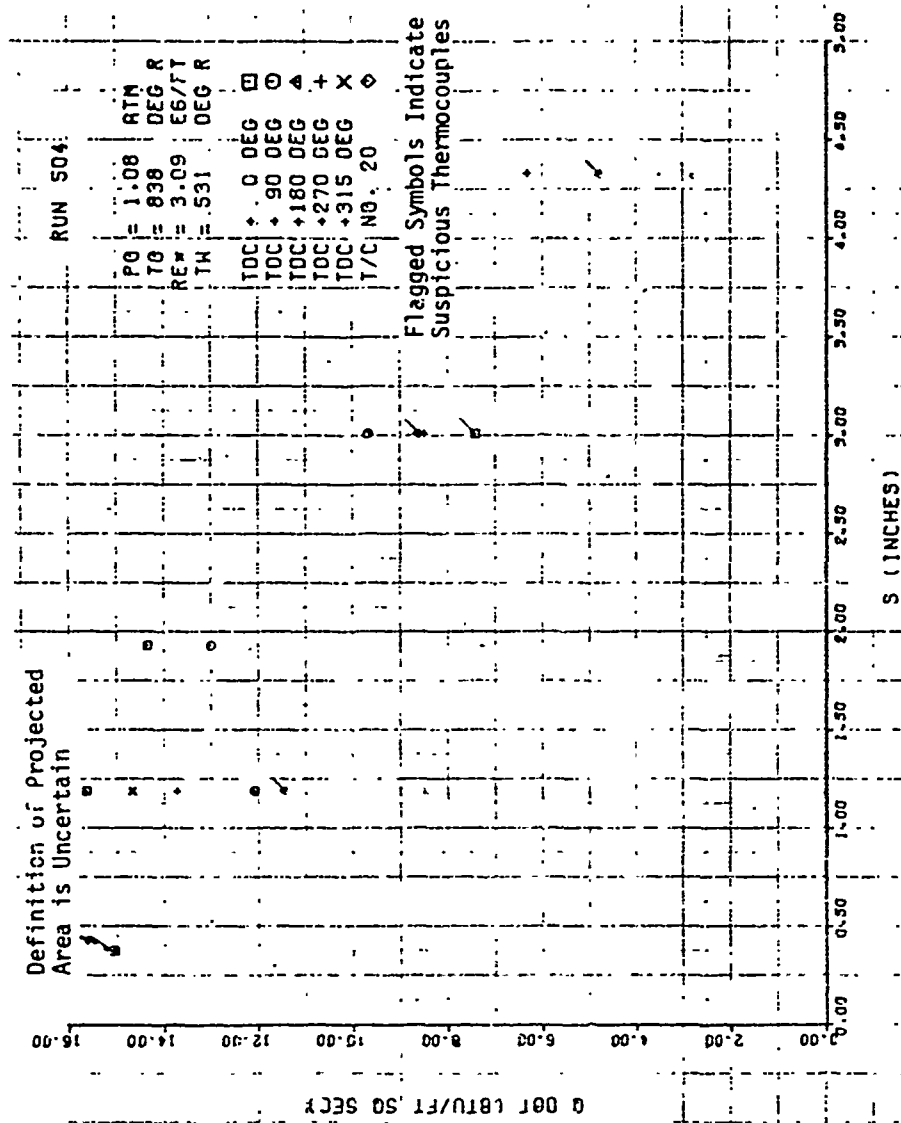


Figure 6-11. Continued

d. Run 504 ($Re_{\infty} = 7.74 \times 10^6/\text{ft}$)

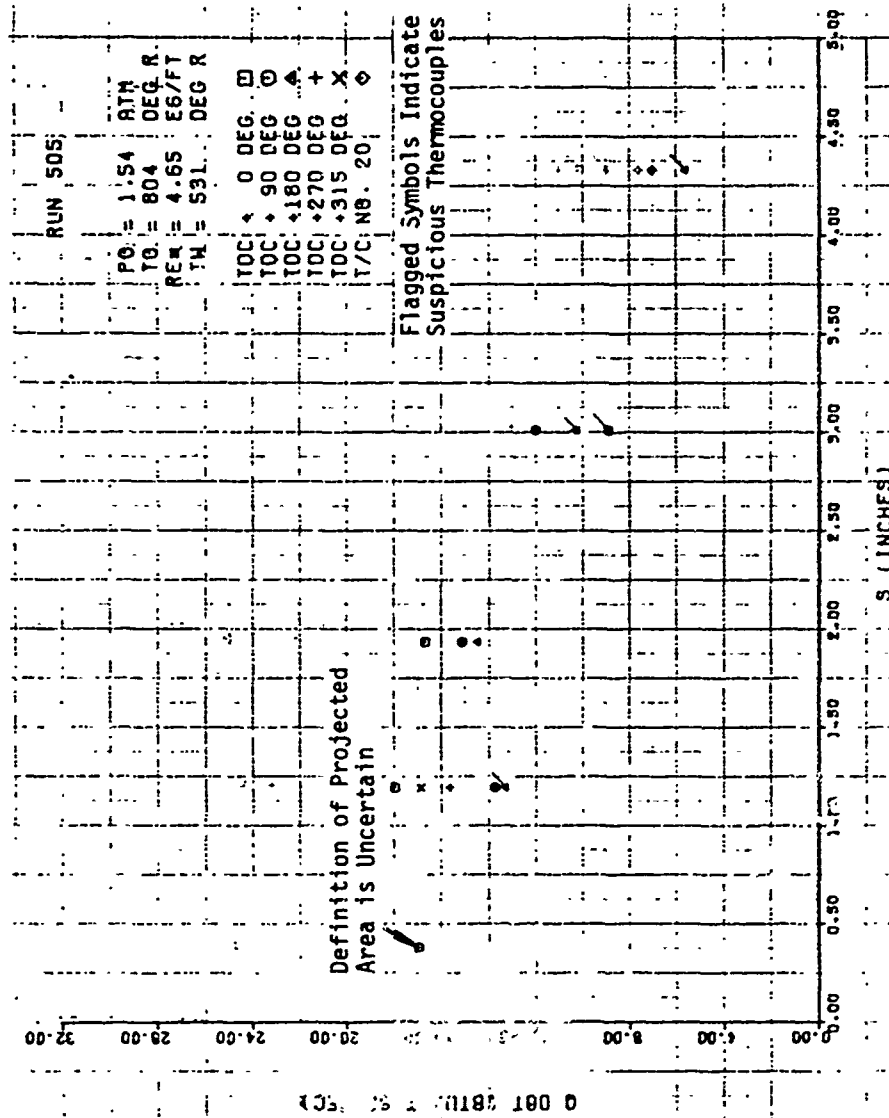


Figure 6-11. Continued

e. Run 505 ($Re_{\infty} = 11.76 \times 10^6/\text{ft}$)

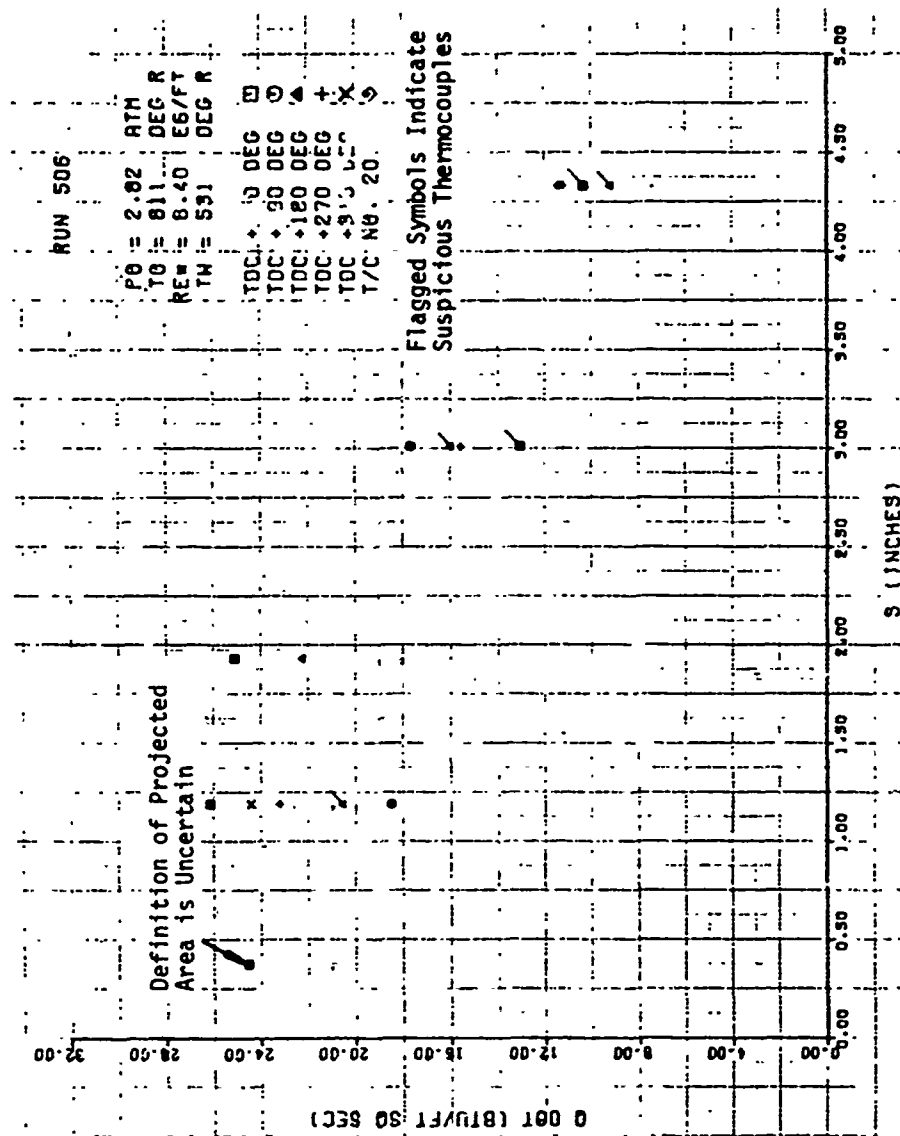


Figure 6-11. Continued

f. Run 506 ($Re_{\infty} = 21.15 \times 10^5/\text{ft}$)

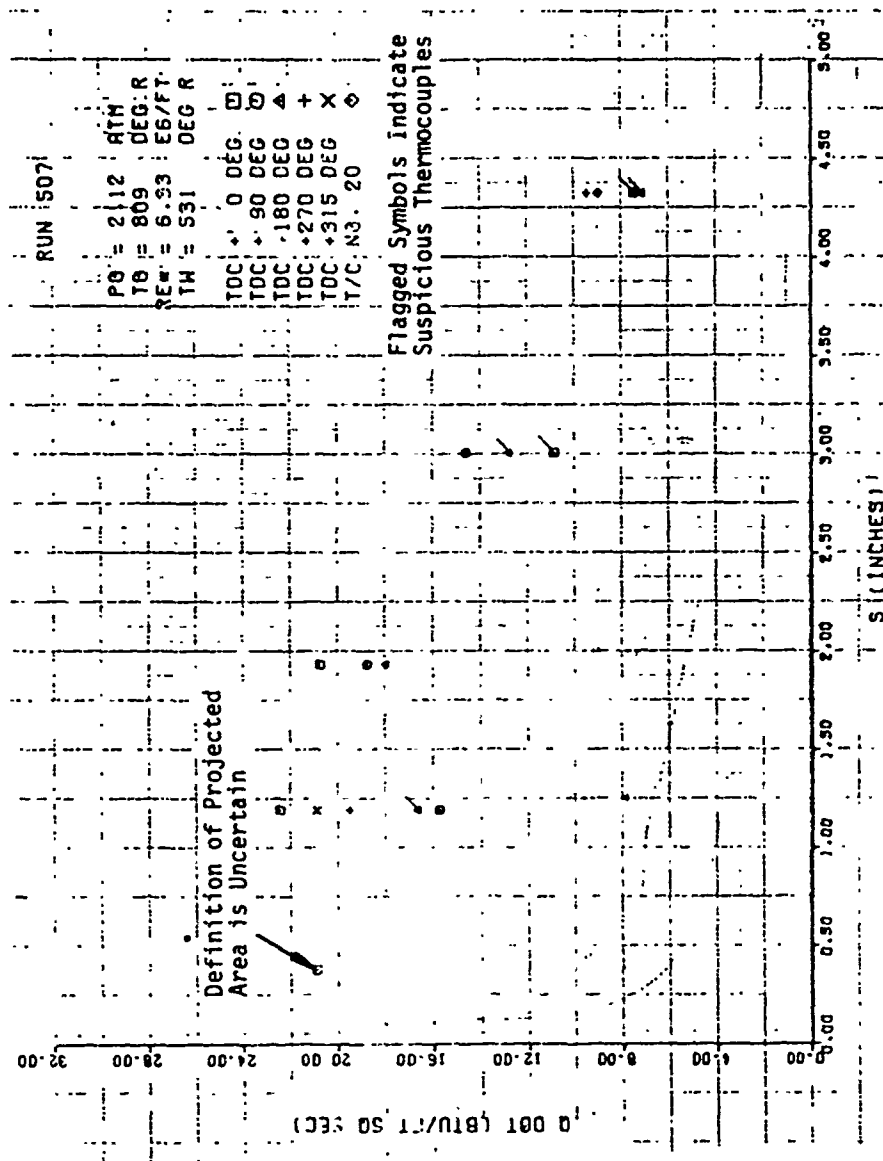


Figure 6-11. Concluded

g. Run 507 ($Re_{\infty} = 15.78 \times 10^6/\text{ft}$)

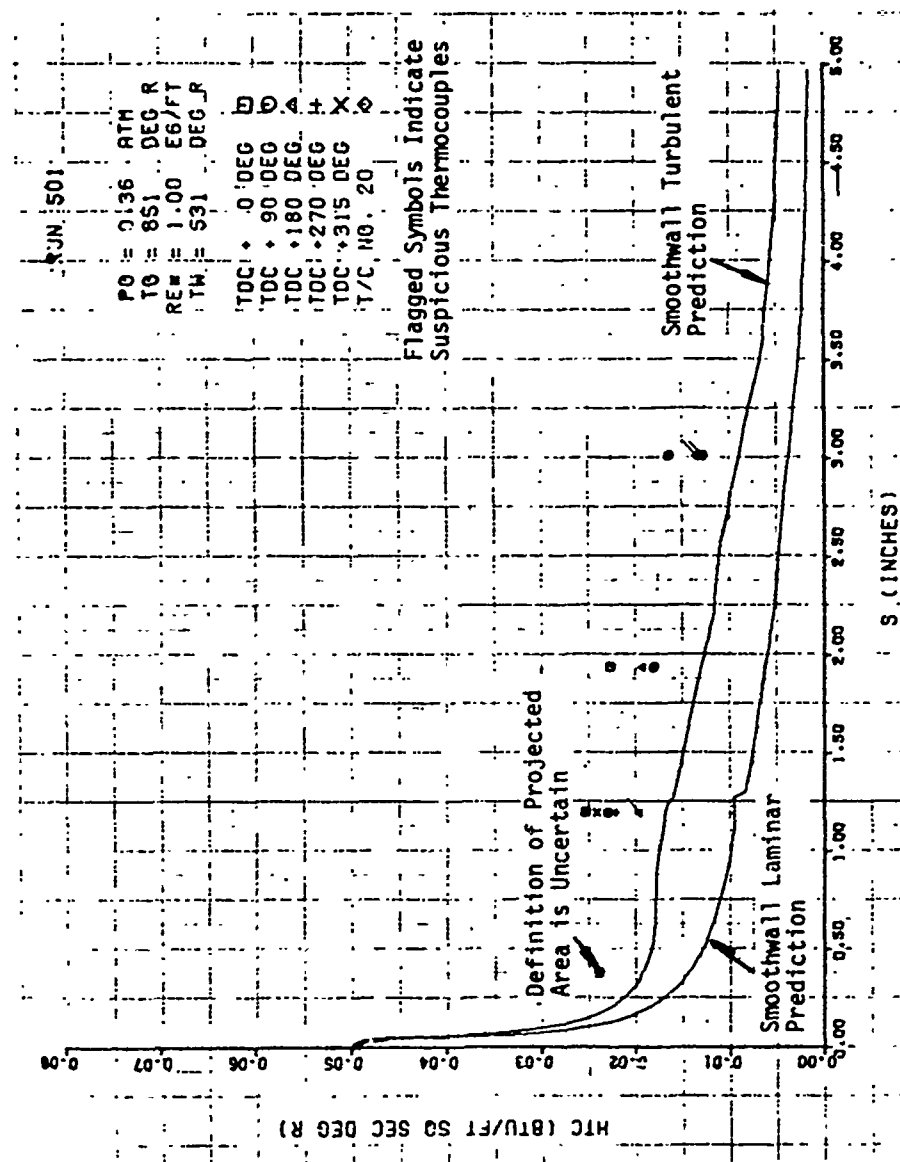


Figure 6-12. Convective Heat Transfer Coefficient Distribution, Scallop Calorimeter Model

a. Run 501 ($Re_{\infty} = 2.61 \times 10^6/\text{ft}$)

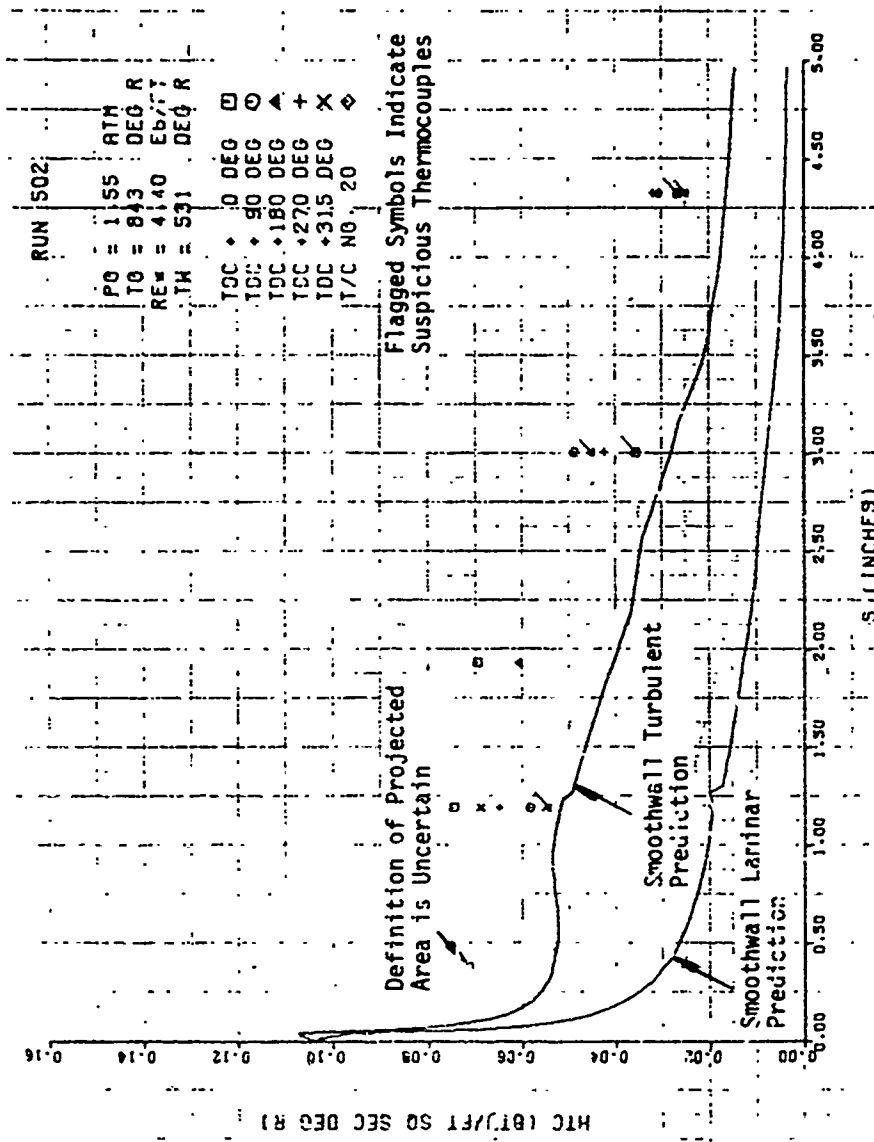


Figure 6-12. Continued

b. Run 502 ($Re_{\infty} = 10.93 \times 10^6/\text{ft}$)

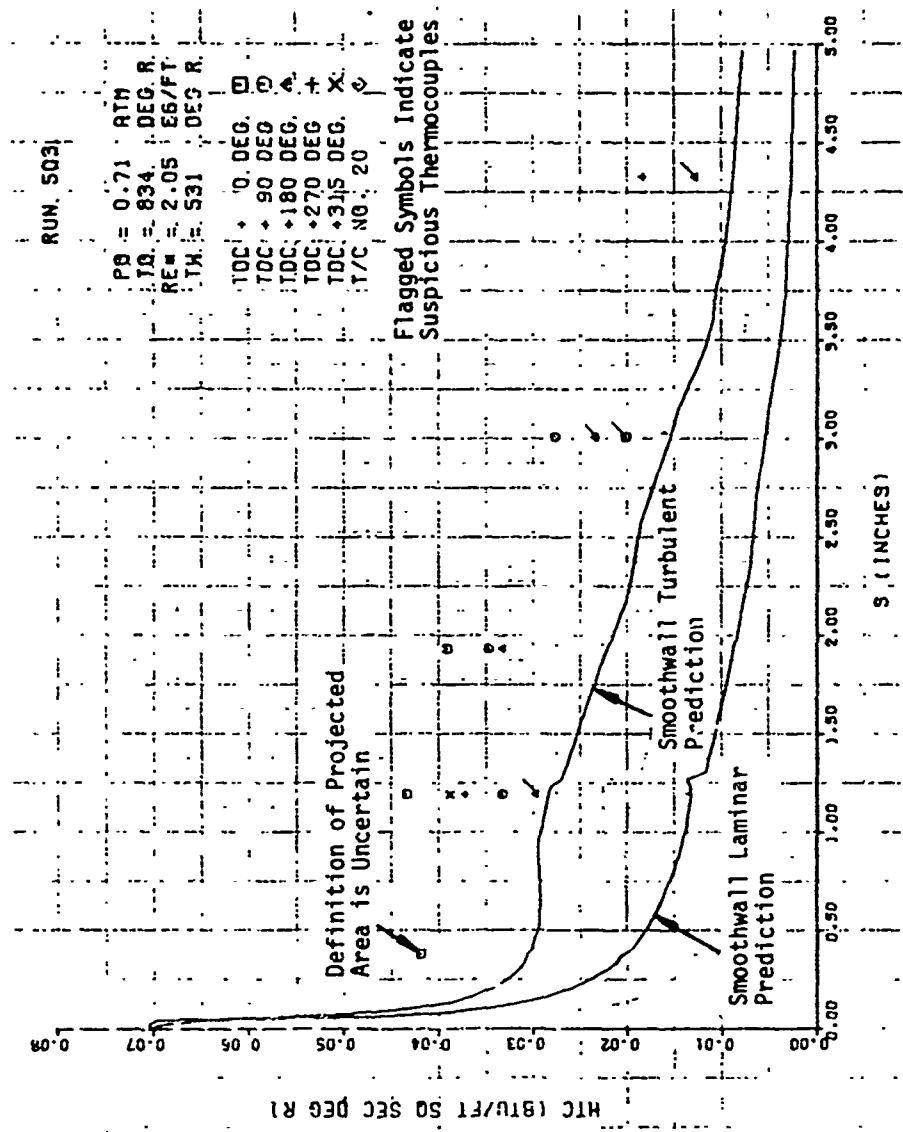


Figure 6-12. Continued

c. Run 503 ($Re_{\infty} = 5.16 \times 10^5/\text{ft}$)

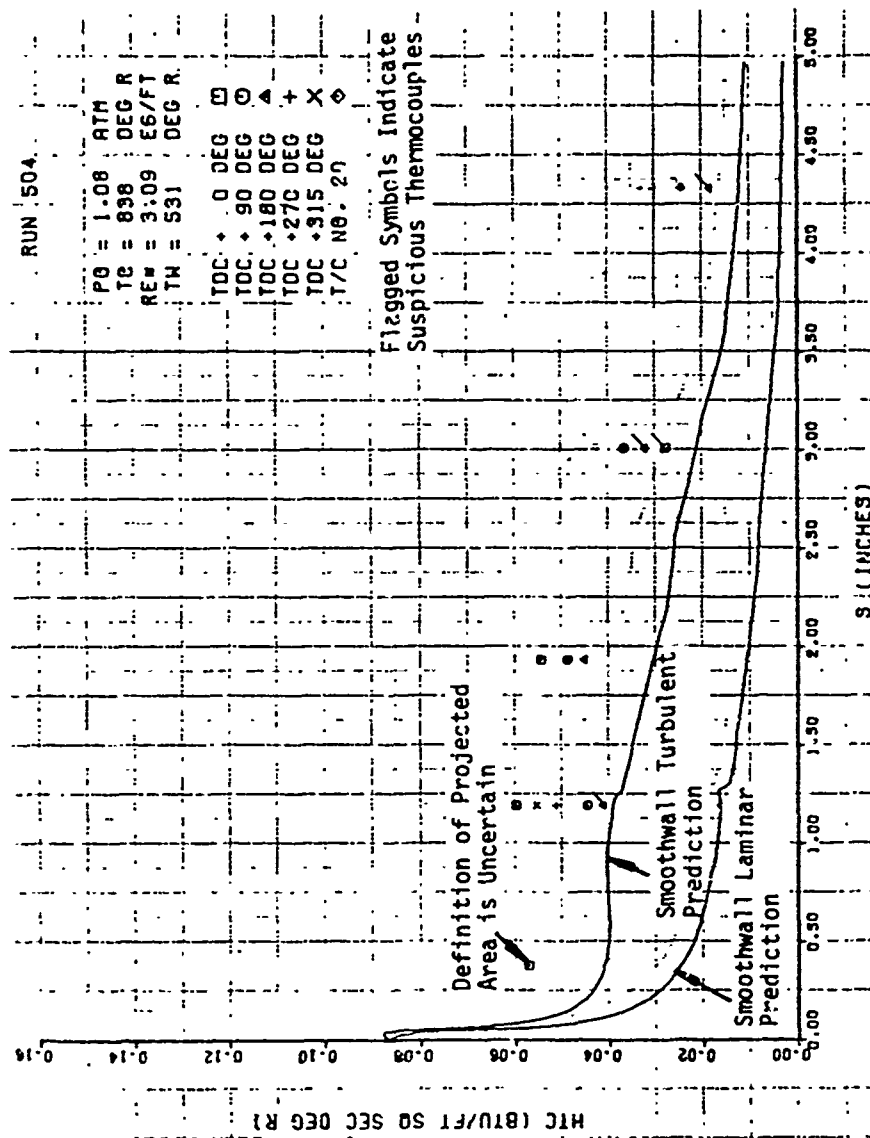


Figure 6-12. Continued

d. Run 504 ($Re_{\infty} = 7.74 \times 10^5/\text{ft}$)

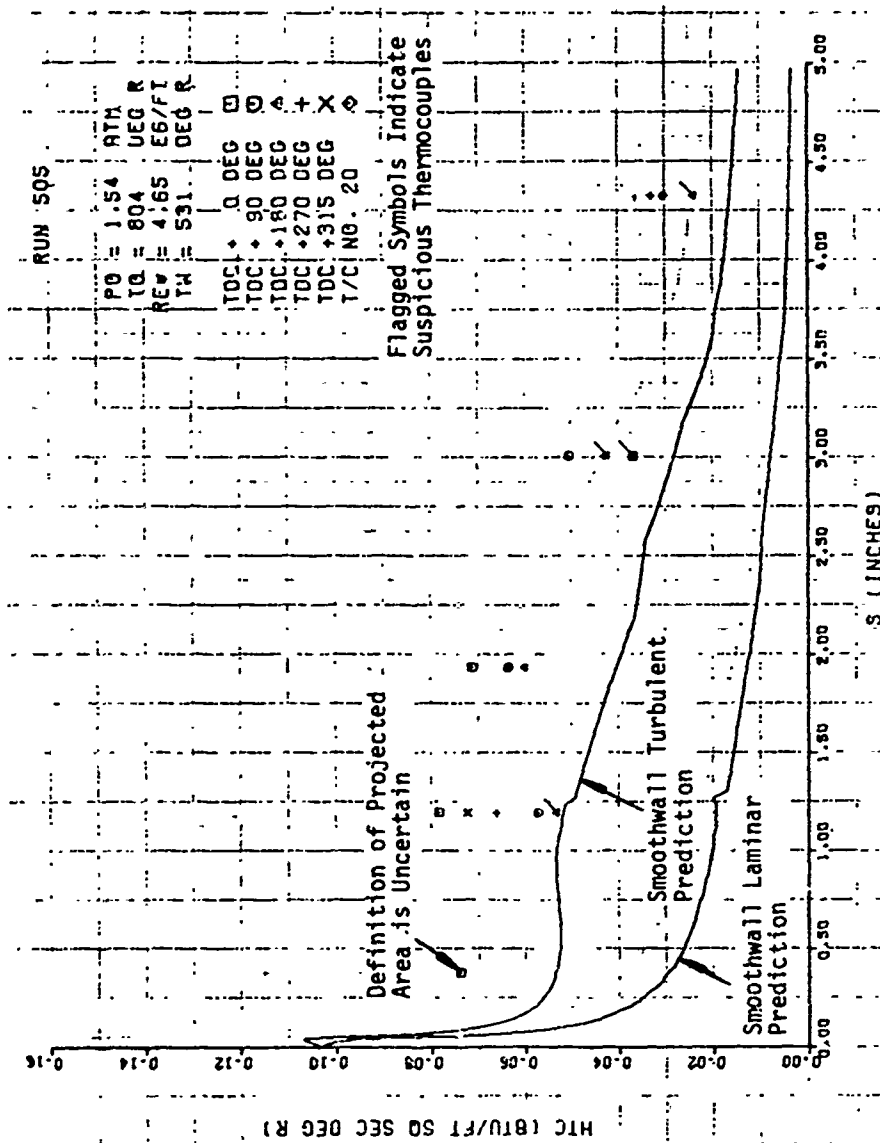


Figure 6-12. Continued

e. Run 505 ($Re_{\infty} = 11.76 \times 10^6 / ft$)

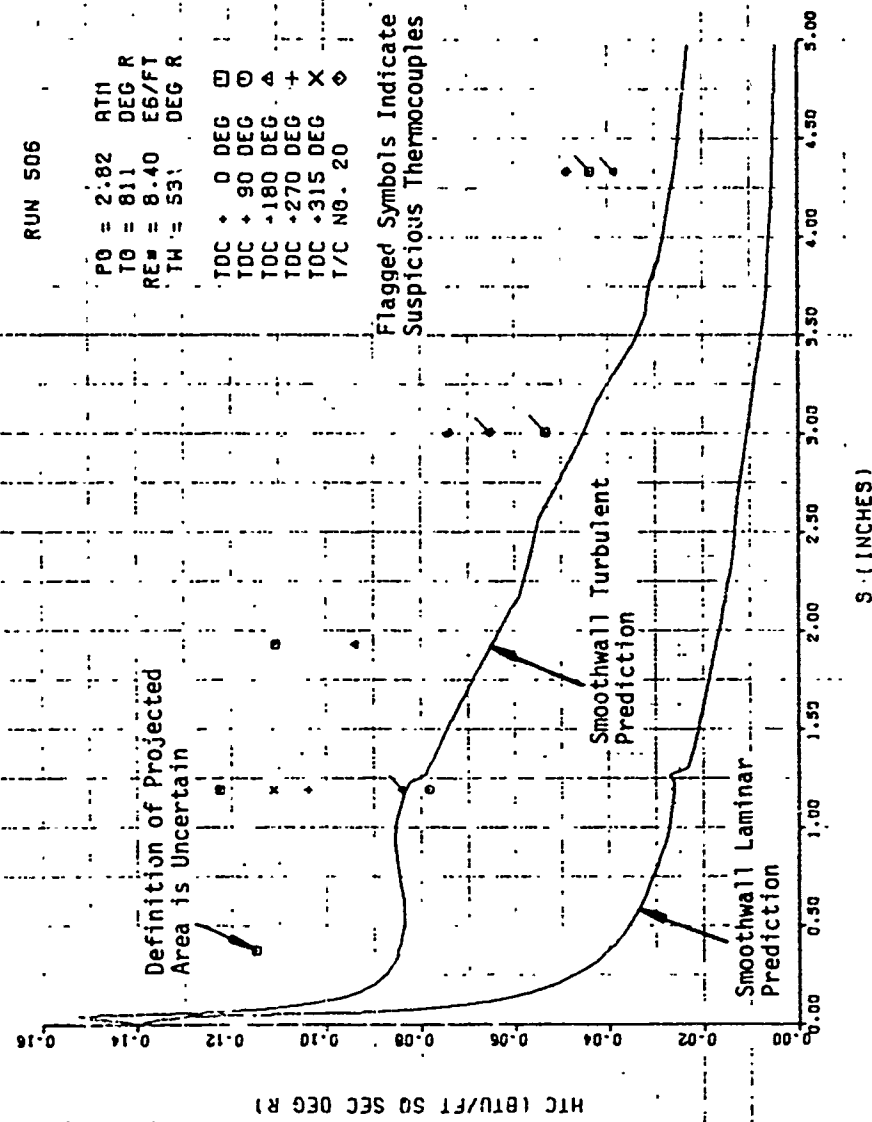


Figure 6-12. Continued

f. Run 506 ($Re_{\infty} = 21.15 \times 10^6/\text{ft}$)

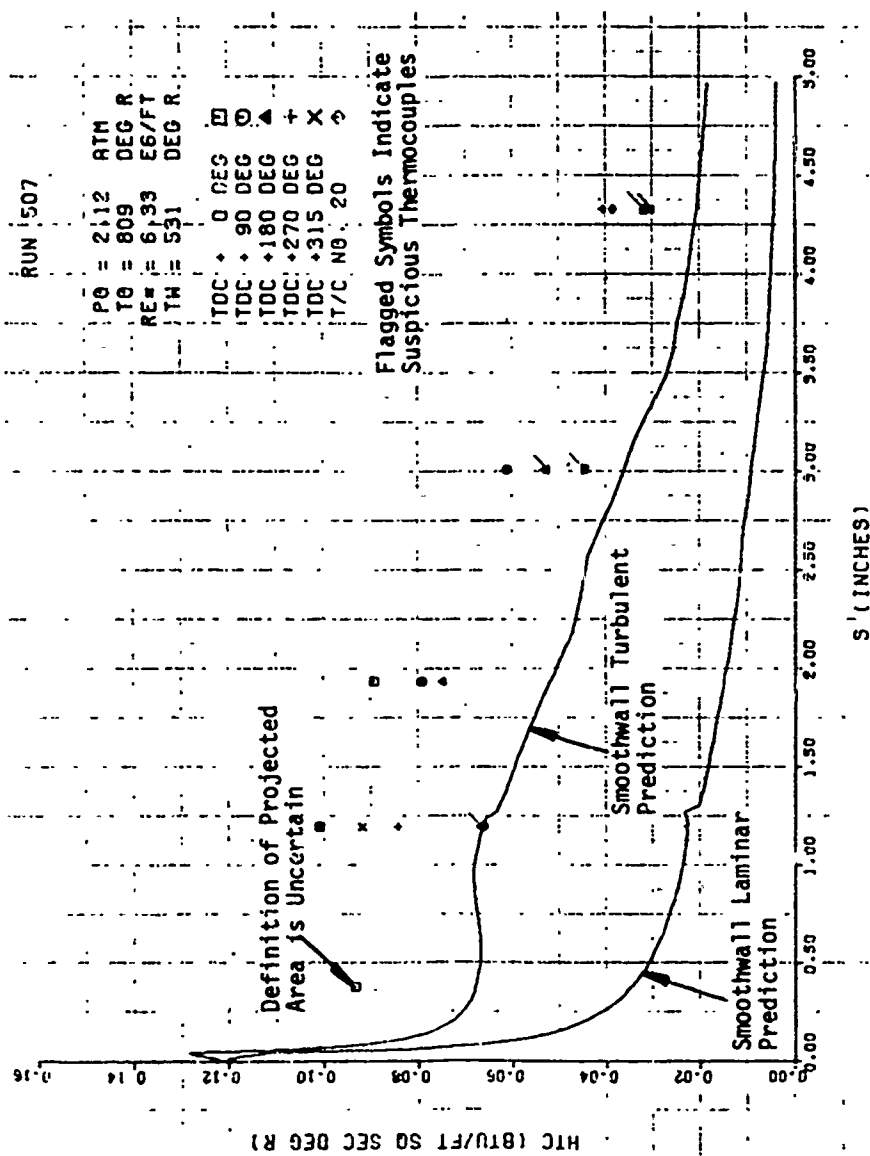


Figure 6-12. Concluded

g. Run 507 ($Re_{\infty} = 15.78 \times 10^6/\text{ft}$)

SECTION 7

RESULTS AND CONCLUSIONS

In this section the reduced data presented in Section 6 are compared with anticipated results. In Section 7.1 the data for the baseline Reynolds number condition are compared with heat transfer rates inferred from low temperature ablator (LTA) recession data. Comparison of all of the reduced data with the PANT derived sand grain roughness heat transfer correlation is shown in Section 7.2, and, in Section 7.3, preliminary conclusions are drawn from these comparisons.

7.1 COMPARISON WITH INFERRED HEATING

The scallop calorimeter model is a replica of the final ablated shape of PANT Series D Run 201. Run 201 was a camphor low temperature ablator (LTA) model which was tested at a freestream Reynolds number (Re_∞) of $10 \times 10^6/\text{ft}$ and total temperature (T_0) = 585°F. In the Series H environmental test plan (Reference 7) a technique was described for inferring the heat transfer coefficient distribution on an ablating body given the surface thermochemistry, and the pressure, recovery temperature, and normal recession rate distribution. The most important of these parameters is the recession rate since inferred heating is directly proportional to measured recession rate. In Reference 7 a preliminary inferred heat transfer coefficient distribution was calculated for Run 201 assuming the model shape to be completely steady. In reality, however, small changes in body shape do occur in the stagnation region and on the aft cone and hence the local recession rate cannot, at all times during the test, be related to the stagnation point rate.

In order to more accurately infer the heating distribution to the final shape of Run 201 measurements of the forecone off centerline recession rate were performed. Specifically 16mm overhead close-up movie film was used to measure the axial recession rates for the stagnation point and two points located 1.0 inch off the model centerline on either side of the stagnation point. In addition measurements of the aftcone radial recession rate were taken from the 35mm overhead photographs. These measurements were taken since it was noted that over the span of the test the aftcone angle was gradually increasing indicating a nonuniform recession rate distribution over the aftcone.

The axial and radial recession rates are related to the normal recession rate through

$$\begin{aligned}\dot{s} &= \dot{z} \sin \theta \\ \dot{s} &= \dot{r} \cos \theta\end{aligned}\tag{7-1}$$

where \dot{s} = normal recession rate

\dot{z} = axial recession rate

\dot{r} = radial recession rate

θ = surface slope relative to body centerline ($\theta = 90^\circ$ at the stagnation point)

the measurement of the local surface body angle is subject to uncertainty because of the scalloped surface and also because of slight model asymmetries. Figure 7-1 presents a plot of surface slope versus streamwise location for the final shape of Run 201 indicating the level of uncertainty in this measurement. The surface angle distribution used in the heating predictions shown in Section 6 represents the average of the uncertainty band.

The surface slope distribution combined with the measured axial or radial recession rates gives an estimate of the surface normal recession rate distribution, Figure 7-2 shows this plot. The uncertainty in the data points comes from uncertainty in both the local surface slope and the measured recession rate (axial or radial). The best estimate of the actual recession rate distribution is based on a fairing between the steady shape distribution and the measured aftcone data points.

The recession rate distribution (Figure 7-2) is then combined with the pressure and recovery temperature distributions (Figures 6-7 and 6-8) using the technique described in Reference 7 to determine an inferred heat transfer coefficient distribution, which is shown in Figure 7-3.

In order for one to compare the inferred heating distribution with the calorimeter data, the inferred heating must be corrected to account for differences in supply temperature (T_o) and pressure (P_{t2}) between the LTA and the calorimeter tests. This correction was obtained using the smoothwall turbulent heating model in the PANT computer code. That is,

$$h_{\text{low } T_o \text{ inferred}} = h_{\text{high } T_o \text{ inferred}} \left(\frac{h_{\text{low } T_o}}{h_{\text{high } T_o}} \right)_{\text{PANT code}}\tag{7-2}$$

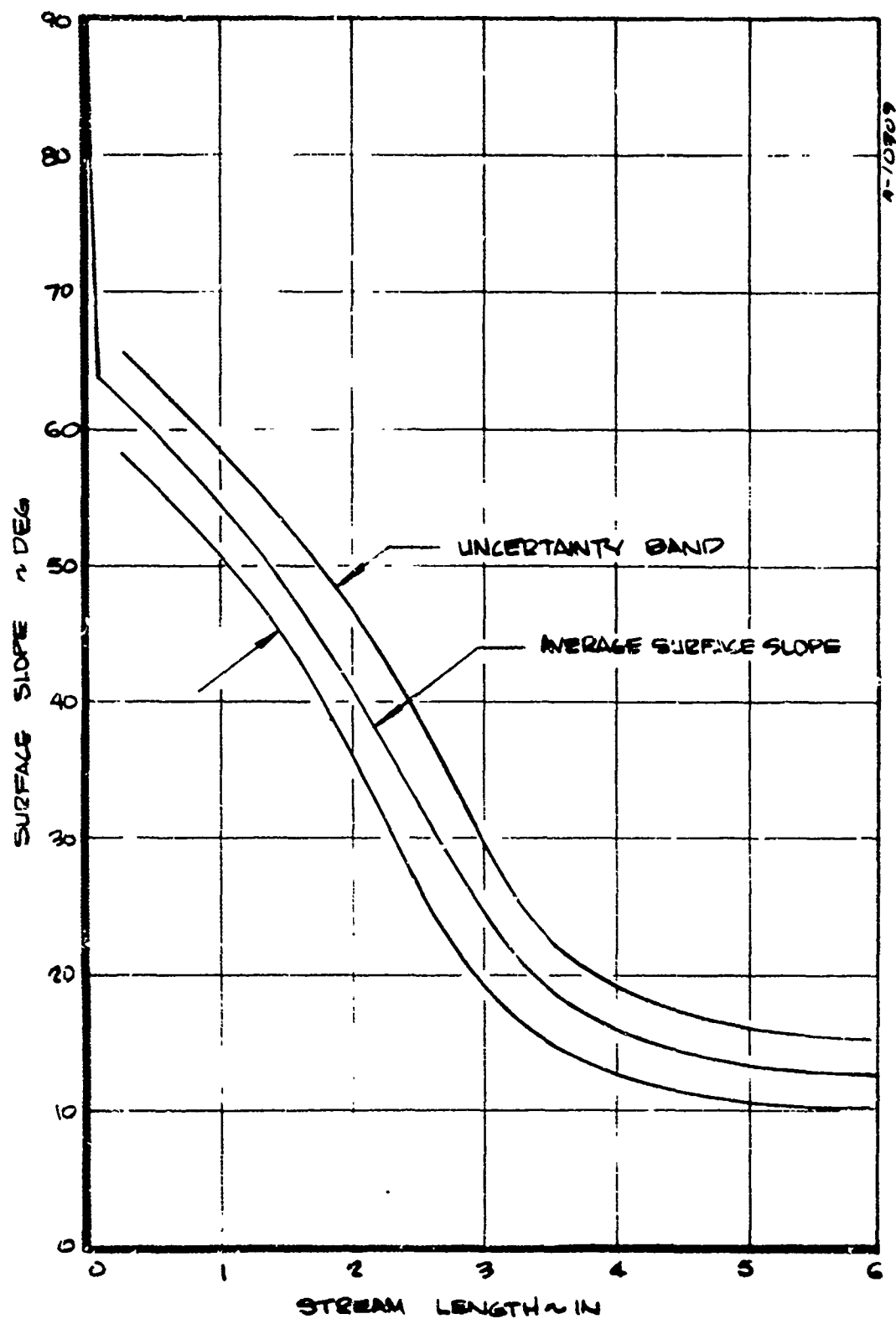


Figure 7-1. Surface Slope Distribution for the Final Shape of Run 201

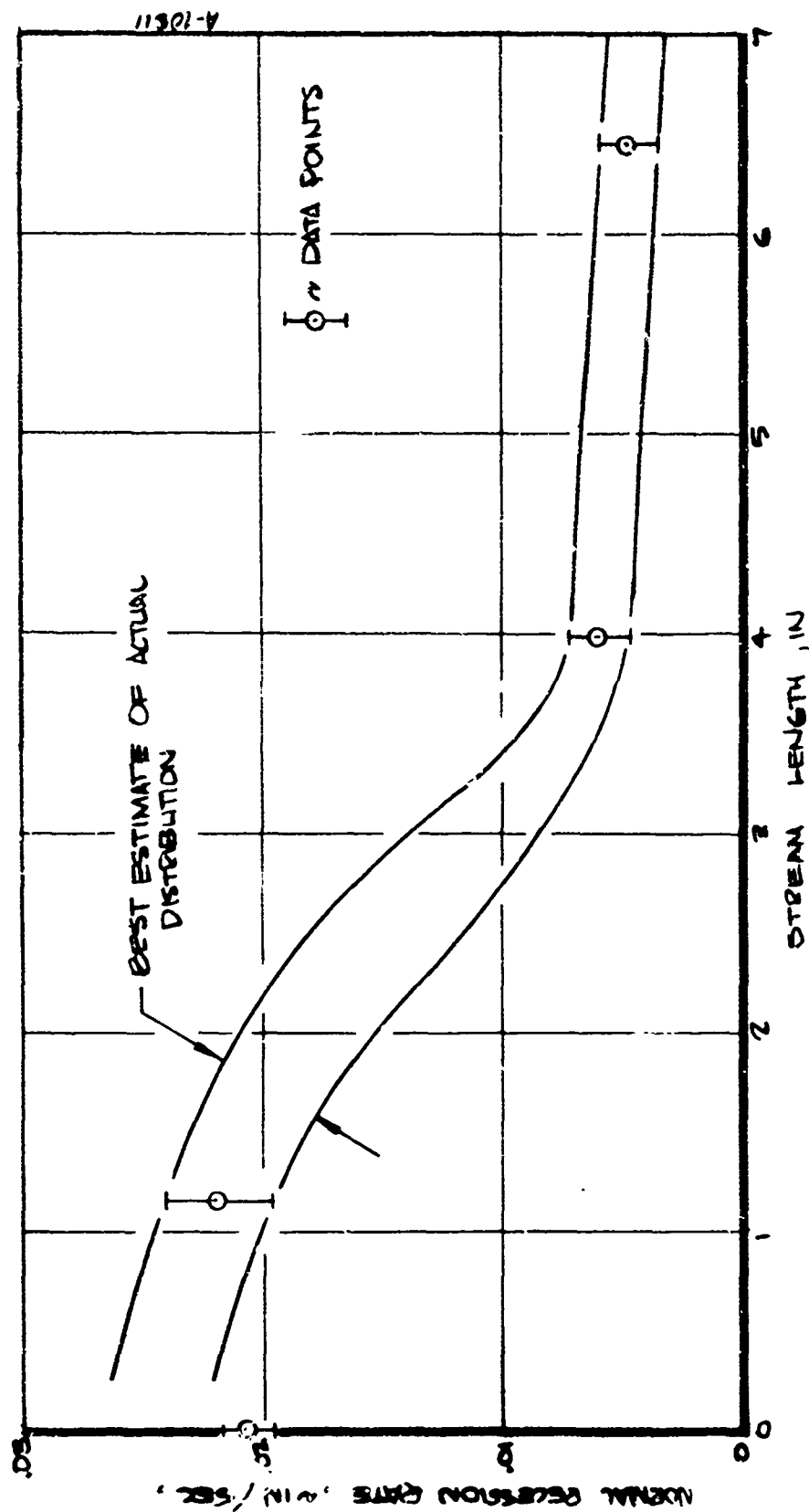


Figure 7-2. Measured Recession Rates and Best Estimate of Normal Recession Rate Distribution for the Final Time of Run 20.

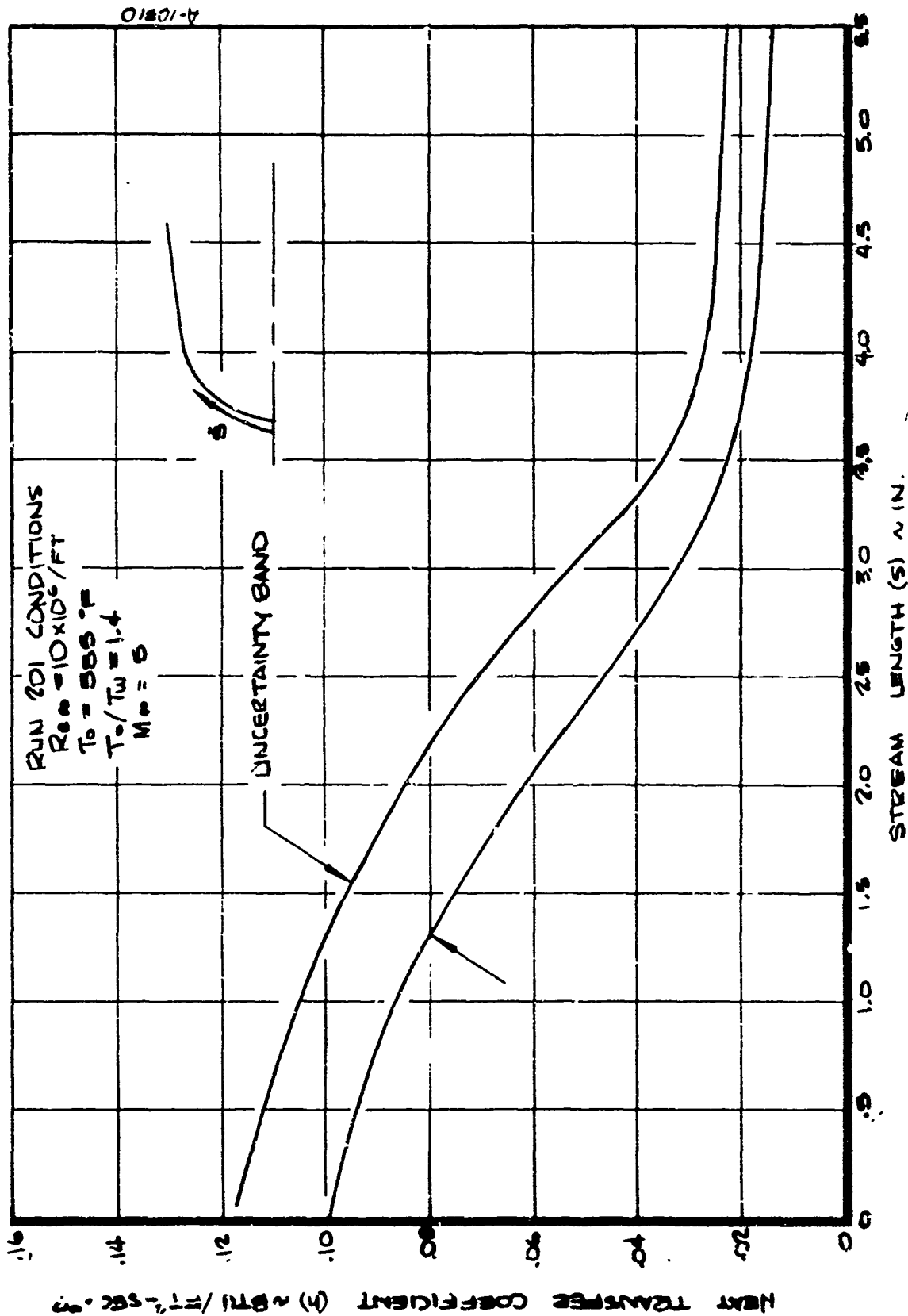


Figure 7-3. Inferred Distribution of Nonblown Heat Transfer Coefficient for the Final Shape of Run 201

where

$h_{\text{low } T_o}$
inferred - is the transfer coefficient corresponding to the low T_o calorimeter test conditions

$h_{\text{high } T_o}$
inferred - was derived from LTA recession data and is shown in Figure 7-3.

$\left(\frac{h_{\text{low } T_o}}{h_{\text{high } T_o}} \right)_{\text{PANT code}}$ - is the ratio of smoothwall transfer coefficient values from PANT code predictions for the calorimeter shape

The correction does not account for changes in roughness heating augmentation between the two test conditions. It is not known what the change in augmentation is. However, if the trends given by the PANT sand grain roughness effects correlation apply, the change in augmentation should be small at the 10×10^6 /ft Reynolds number conditions.

Figure 7-4 shows a comparison of the resulting inferred distribution to the calorimeter data for Run 502 ($Re_\infty = 10 \times 10^6$ /ft). The boxed areas around the calorimeter data indicate the spread in the data on a given ring and the streamlength covered by each ring. Because the rings are insulated from one another the measured heat flux represents an average of the local heat flux over the ring.

The data are in general agreement with inferred heat coefficients from the LTA data. The calorimeter data on the forecone (Rings 2, 3, and 4) agree well with the inferred heat transfer but the aftcone data (Ring 5) is higher than the inferred.

7.2 COMPARISON WITH PANT ROUGH WALL HEATING CORRELATION

Under the PANT program a rough wall heating correlation applicable to sandgrain type surface roughness was developed (Reference 8). In this correlation the roughness heating augmentation factor

$$K_r = \frac{h_{\text{rough}}}{h_{\text{smooth}}} \quad (7-3)$$

is correlated versus a parameter which is approximately proportional to the ratio of the roughness height to the laminar sublayer thickness:

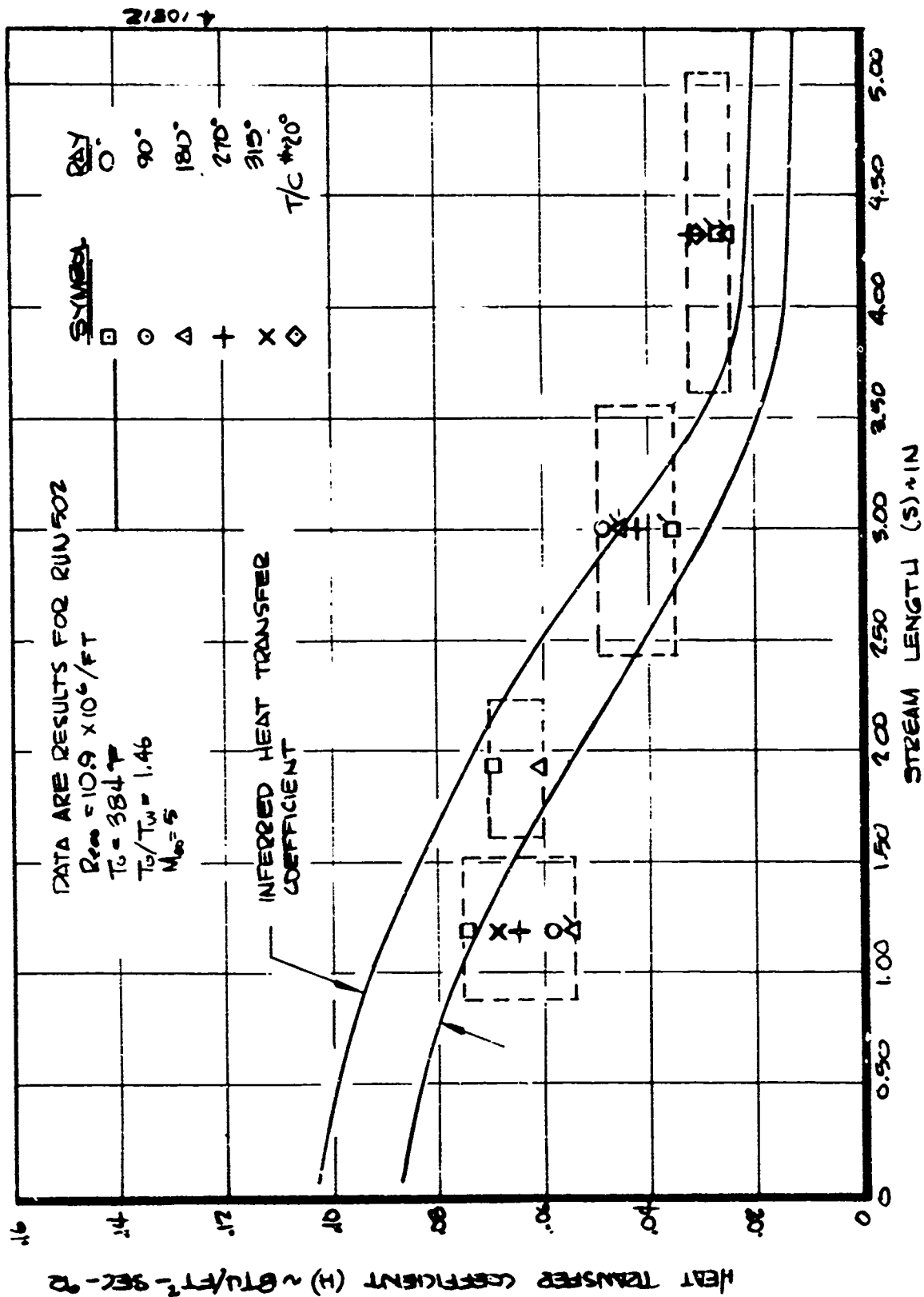


Figure 7-4. Comparison of Inferred and Measured Heat Transfer Coefficient Distribution for the Baseline Reynolds Number Condition (Run 502)

$$\frac{k}{\delta_{SL}} \propto Re_k \sqrt{C_{H_S}} \left(\frac{T_e}{T_w} \right)^{1.3} \quad (7-4)$$

where k = sandgrain roughness height
 δ_{SL} = laminar sublayer thickness
 $Re_k = \frac{\rho_e u_e k}{\mu_e}$ = boundary layer edge Reynolds number based on roughness height
 C_{H_S} = smoothwall Stanton number
 T_e = local boundary layer edge temperature
 T_w = local wall temperature

A comparison of the Series H calorimeter data with the PANT roughwall heating correlation is shown in Figure 7-5. The value of K_r for each data point was calculated by dividing the measured heat transfer coefficient by the smoothwall, turbulent PANT code prediction. The error bands on each K_r represent the spread in the data. The data points flagged as suspicious in Section 6 were not included in these error bands. The abscissa is

$$Re_e \sqrt{C_{H_S}} \left(\frac{T_e}{T_w} \right)^{1.3} \text{ mils}^{-1} \quad (7-5)$$

where

$$Re_e = \frac{\rho_e u_e}{\mu_e}$$

Therefore, the PANT correlation appears as a series of parallel lines, one for each roughness height. The value of the abscissa parameter for each data point was taken from the smoothwall predictions. Different symbols are shown for each wind tunnel run. For each run, K_r was found to be about 1.3 on the fore-cone ring (Ring 2), increases to about 1.6 on Rings 3 and 4; and further increases to approximately 2.0 on Ring 5. This observation is consistent with the fact that scallop dimensions are greater on the aftcone than on the fore-cone. The point of interest is that the heating increase factor on each ring is not sensitive to the test Reynolds number. The measured heating rates scale closely to changes in smoothwall turbulent heating. This demonstrates that the scallops affect heat transfer in a different way than do sand grain roughness elements and tends to confirm the speculation stated in Reference 8 that the

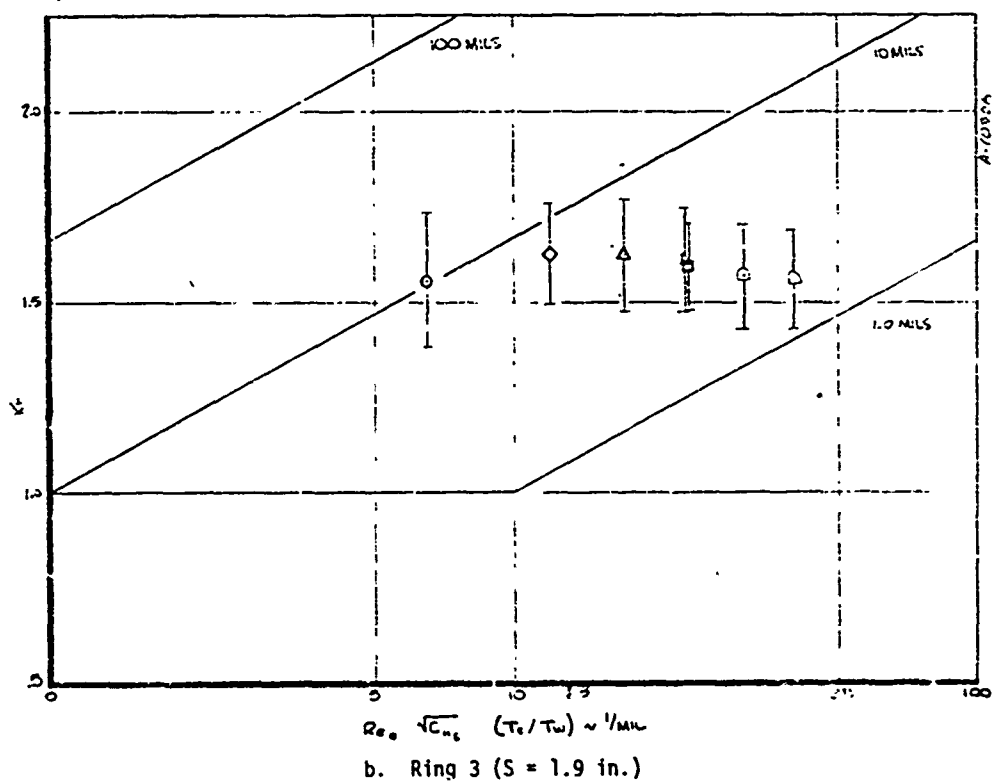
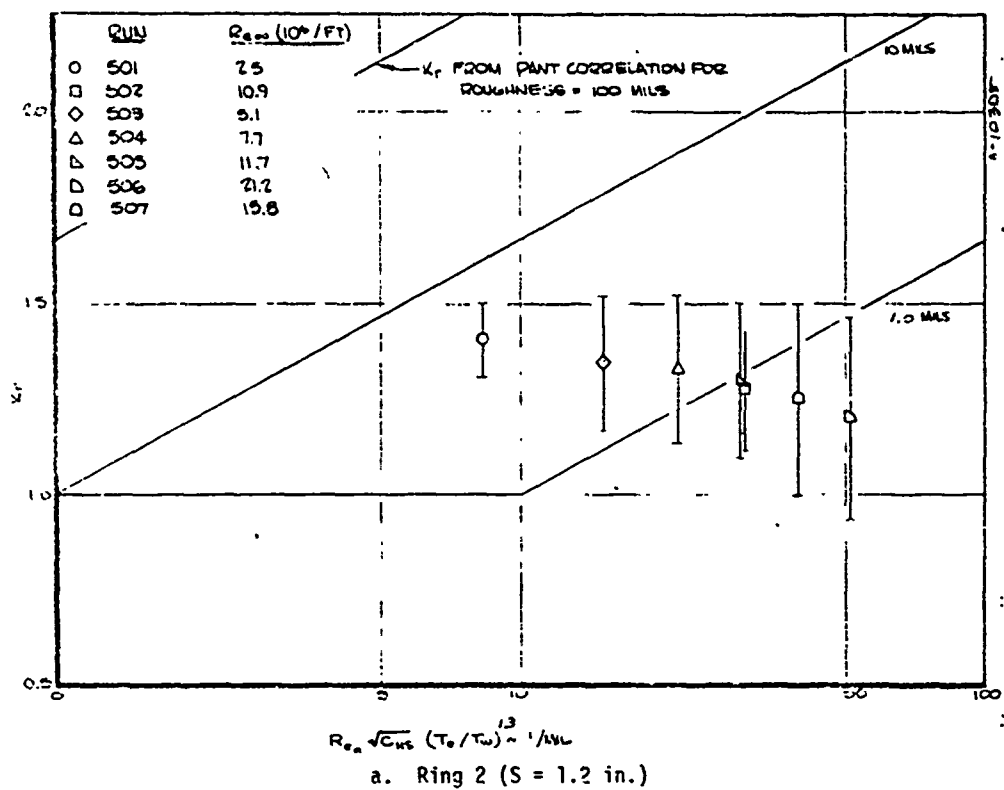


Figure 7-5. Comparison of the Series H Calorimeter Data with the PANT Rough-wall Heating Correlation

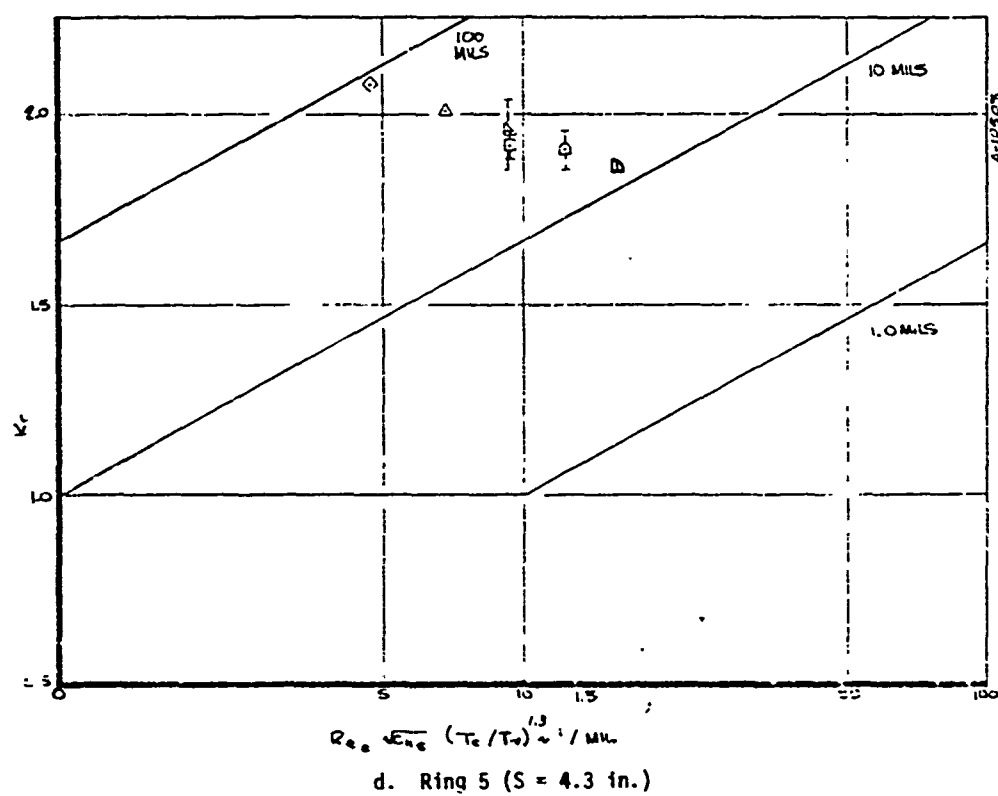
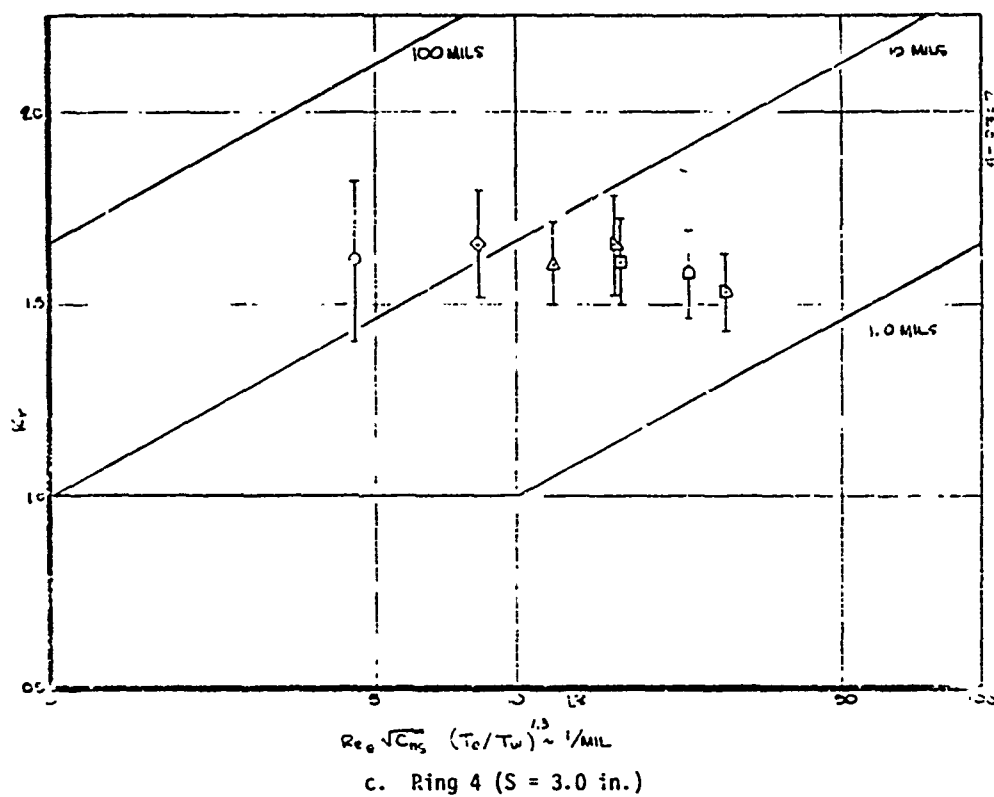


Figure 7-5. Concluded

PANT roughness effects correlation is not directly applicable to scalloped surfaces. Indeed, since scallops form as a result of turbulent flow/material ablation interactions, it would not be expected that a correlation of sand grain heating data would also correlate scallop heating data.

Since the augmentation is insensitive to Reynolds number condition, one might conjecture that scallops affect heating mainly through changes in the inviscid flow rather than through changes in the boundary layer. The shadowgraphs shown in Figure 5-2 confirm that significant surface/shock layer interactions did occur in the calorimeter tests. Similar interactions were observed in shadowgraphs from the Series D and Series I LTA tests.

7.3 CONCLUSIONS AND RECOMMENDATIONS

The following conclusions are drawn from observation of the data and comparison with predictions.

- The consistent ordering of the data on each ring indicates that local variation in the wall thicknesses are different than the average thicknesses used for data reduction.
- The heat transfer to the scalloped surface calorimeter was greater than corresponding smooth wall predictions.
- The measured heat transfer rates agree generally with heating rates inferred from the baseline LTA model.
- The roughness augmentation factors (K_r) for each scallop calorimeter ring do not scale with the correlation parameter

$$Re_e \sqrt{C_{H_S}} (T_e/T_w)^{1.3}$$

as would be expected from the PANT sand grain roughness effects correlation.

- The roughness augmentation factor (K_r) distribution around the body is nearly independent of Reynolds number but increases with increasing scallop roughness height.

The above conclusions indicate that there exists significant differences between the roughwall heat transfer effects caused by sand grain roughness and those caused by scallop roughness. It is conjectured that scallops increase surface heat transfer rates primarily through surface/shock layer interactions. It may also be speculated that the measured heat flux is higher than the inferred heat flux on the aftcone (e.g., Figure 7-4) because of the effects

of the upstream mass addition during the ablation test. In other words perhaps for the ablating case (i.e., the inferred) the mass addition to the boundary layer on the forecone has thickened the mass transfer boundary layer and hence reduced the ablation rate along the aftcone surface. The data appear, therefore, to indicate that relevant information can be derived from comparisons between camphor wind tunnel ablation tests and replica calorimeter tests.

It is recommended that boundary layer heat and mass transfer analysis be performed to assess the effect of the mass transfer on the cone surface ablation conditions. Once the differences between inferred heating rates and calorimeter heating data are resolved, it is recommended that heating rates be inferred from camphor model tests and used to evaluate the effects of scallops on heat transfer.

REFERENCES

1. Abbett, M. J., et. al., "Unsteady Flow on Ablated Nosetip Shapes," Aero-therm Report 73-87, Aerotherm Division/Acurex Corporation, December 1973.
2. "The Thermal Conductivity and Specific Heat of a Cast 356 Aluminum Alloy," Dynatech Corporation Final Report to Acurex Corporation., P. O. 22333, February 13, 1974.
3. Baltakis, F. D., "Performance Capability of the NOL Hypersonic Tunnel," NOI-TR 68-187, October 1968.
4. "User's Manual, Aerotherm Charring Material Thermal Response and Ablation Program, Version 3, Volume 1", Aerotherm Report UM-70-14, TR-70-92, April 1970.
5. Anderson, A. D., "Passive Nosetip Technology (PANT) Program, Interim Report, Vol. III - Surface Roughness Effects, Part III - Boundary Layer Transition Data Correlation and Analysis," Aerotherm Report 74-90, Aerotherm Division, Acurex Corporation, January 1974.
6. Wool, M. R., Overly, P. T., and Derbidge, T. C., "Passive Nosetip Technology (PANT) Program, Interim Report, Vol. VII - Computer User's Manual, Steady-State Analysis of Ablating Nosetips (SAANT) Program", Aerotherm Report 74-90, Aerotherm Division, Acurex Corporation, January 1974.
7. Derbidge, T. C., Nardo, C. T., and Overly, P. T., "An Experimental Study to Evaluate Heat Transfer Rates to Scalloped Surfaces", Aerotherm C/N 70-40.356, Aerotherm Division/Acurex Corporation, December 1973.
8. Powars, C. A., "Passive Nosetip Technology (PANT) Program, Interim Report, Vol. III - Surface Roughness Effects, Part II - Roughness Augmented Heating Data Correlation and Analysis", Aerotherm Report 74-90, Aerotherm Division/Acurex Corporation, January 1974.